A simple developmental model recapitulates complex wing venation patterns in insects
Supplemental Materials

Jordan Hoffmann[†,1], Seth Donoughe[†,2], Kathy Li[3], Mary K. Salcedo[2], Chris H. Rycroft[1,4]

Contents

[†] Jordan Hoffmann and Seth Donoughe contributed equally to this work. Author order is random.
1 Paulson School of Engineering and Applied Sciences, Harvard University, Cambridge, MA 02138, United States
2 Department of Organismic and Evolutionary Biology, Harvard University, Cambridge, MA 02138, United States
3 Applied Physics and Applied Mathematics Department, Columbia University, New York, NY 10027, United States
4 Computational Research Division, Lawrence Berkeley Laboratory, Berkeley, CA 94720, United States

Overview of this document

We have divided this supplement into six main sections: (1) Data collection, image processing, and segmentation, (2) Quantitatively characterizing the arrangement of wing veins, (3) Procedure for simulating secondary vein patterns, (4) Simulation results, (5) Availability of data and code, and (6) Acknowledgements for images obtained from published books.

1   Data collection, image processing, and segmentation

The dataset of insect wings studied in this paper is a combination of original micrographs of wild-collected specimens and published wing tracings from the scientific literature. In this section, we describe our techniques for acquiring those images and a custom computational method that we used to segment the wing veins. We also show that this method is robust and effective for segmenting many different types of biological images. Finally, we assess segmented wing images to confirm that wings from different sources are comparable.

1.1   Original micrographs

Some specimens were collected by the authors in the vicinity of Swarthmore College in Swarthmore, PA or the Concord Field Station, in Bedford, MA. Other specimens were donated from the Harvard University entomology teaching collections. Insects were caught with nets, euthanized, pinned, spread, and identified. Wings were removed with forceps at the wing hinge and then imaged with either a scanner or microscope. *Imaging with a flatmount scanner:* Wings were placed under a glass slide on a film and document scanner (CanoScan 9000F Mark II), illuminated with white reflected light, and then scanned at a resolution of 2400 dots per inch (DPI). *Imaging with a microscope:* Wings were illuminated with transmitted white light and imaged with a Zeiss AxioZoom V16 microscope at $35\times$ optical magnification. Using Zen Pro software (Zeiss), the stage was moved to tile the entire wing with overlapping imaging positions. A

Z-stack was captured at each position. Z-stacks were fused using the "Tiling" and "Extended Depth of Focus" functions in `Fiji/ImageJ` (NIH).

1.2   Published wing images

We used Google Scholar and Web of Science to compile a maximally inclusive list of candidate books, reviews, and field guides for Odonata. We then pared down the list to those sources that could be obtained as a physical copy, contained descriptions of multiple species, and included detailed wing drawings that were printed at a high enough resolution to resolve even the smallest vein domains [1, 2, 7, 9]. We scanned each wing image from each source at 1200 DPI. In cases where there was notation on the wing diagrams, we used Adobe Photoshop to manually remove the arrows and/or text if it was possible to do so without disturbing the drawn wings veins. Otherwise, graphically annotated wings were discarded. There is a highly conserved vein domain called the pterostigma that is often pigmented. We manually filled this domain in with white pixels to ensure that it properly segmented as a wing domain. For all published wing images, if the length of the wing was given in the text, we used it. When the length of the wing was not listed, we used the length given in *The Encyclopedia of Life* [20]. When multiple wing measurements were listed, we used the mean length.

1.3   Segmenting wing images

Naturalists have used images—drawings, photographs, and micrographs—to capture the shapes and patterns of biological tissues for hundreds of years. Historically, measurements of morphological traits have been made by hand, and it is especially laborious to extract phenotypes from complex biological images in a high dimensional, quantitative way. Software-based image analysis tools have made this process dramatically faster, but most morphological traits are still not readily quantifiable in an automated manner.

Many diverse tissues and patterns take the form of bounded shapes on a surface, such as the edges of cell junctions in epithelia, coat patterning in mammals, and insect wing veins. Thus, the process of taking a bitmap image of bounded shapes and segmenting into "edges" and "background" is a common problem in many disciplines. Several general purpose tools have been created for this purpose, such as the widely used image processing toolbox `Fiji/ImageJ` or the machine learning based tool `ilastik` [10]. Additionally, a few tissue specific segmentation tools have been created [11, 12, 13, 14].

We found that most standard segmentation tools were ineffective for our purpose of segmenting a wide range of images coming from different sources. In Fig. S1 we show a selection of the wing images used in the present study, including micrographs and scans from published sources.[1] Additionally, we wanted our segmentation tool to unambiguously resolve contacts between wing domains, a capability that is not offered by some existing segmentation methods. Therefore, to segment wing images, we developed a custom code based on the fast marching method with a variable background velocity field [17, 18]. We implement it using the open-source `scikit-fmm` python library [19] which solves the Eikonal equation

---

[1] *Note:* Most images used in this study are between 2000 and 4000 pixels along the long axis.
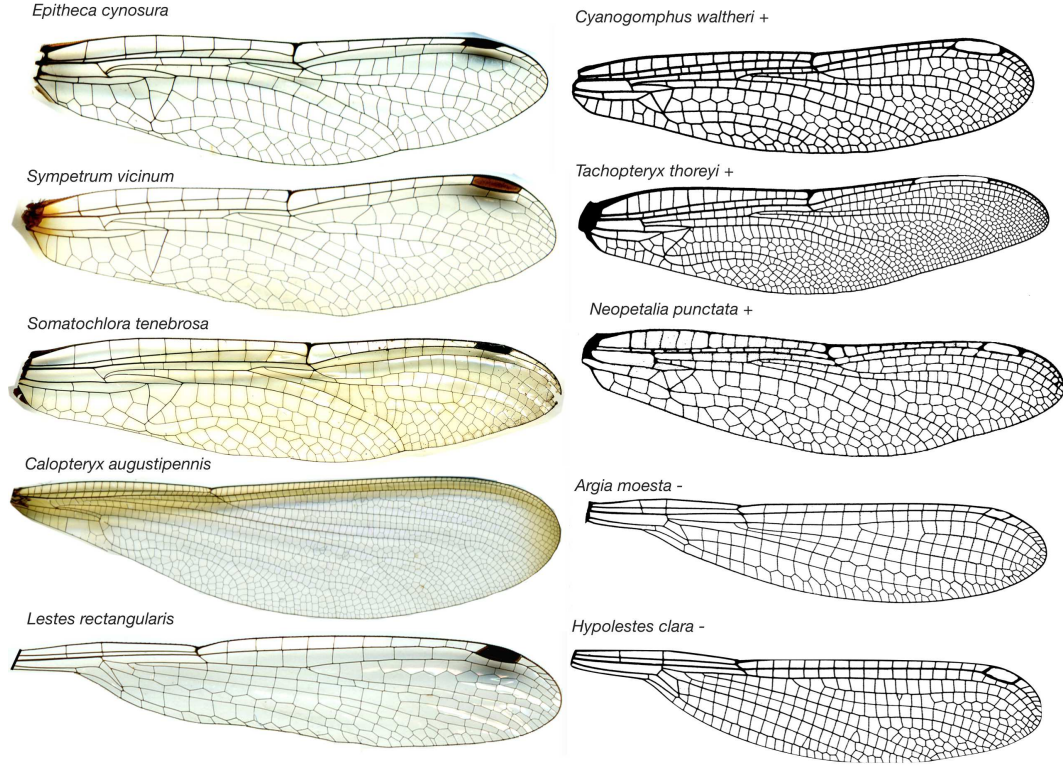
3

Figure S1: **Example wing images used in manuscript.** The left hand column shows wing micrographs reprinted with permission from [8]. Images on the right come from published sources where authors have traced wings. Images marked with '+' are from [2], p. 16, Figure 53; p. 97, Figure 587; p. 100, Figure 604; p. 134, Figure 704; p. 157, Figure 864. (c) 2006 Johns Hopkins University Press. Reprinted with permission of Johns Hopkins University Press. Images marked '−' are reprinted with permission from the artist [7]. Note that in the published wing images, we have filled in the pterostigma domain (typically pigmented) with white pixels to ensure it is properly segmented as a wing domain.

$F(\vec{x})|\nabla T(\vec{x})| = 1$ where $T(\vec{x})$ is the travel time from a set of pre-determined seed points, and $F(\vec{x})$ is a spatially varying speed.

We begin by generating candidate seed points using either a watershed-based segmentation or connected components after Otsu thresholding.[2] Figure S2 outlines the process of our segmentation. Panel **A** shows the original wing image. Panel **B** shows the background velocity field we construct from our image. We threshold the original image and find connected components, each of which is given a different random color in panel **C**. To generate seed points from our connected components, we only include components that have an area of at least 30 pixels, which excludes very small components generated by imaging noise. If a component's dimensions are greater than 500 pixels in both x and y, we treat it as background by randomly dropping a large number of additional seed points in it. We do this in order to chop up the background space and ensure that wing domains do not bleed outside the wing. Remaining connected components are treated as wing domains; the centroid of each domain is assigned a single

---

[2]Which segmentation method we use depends on the type of input image. For published drawings, we used watershed, whereas for micrographs we used Otsu thresholding.

seed at its centroid. Panel **D** shows our seed points as white crosses. From each seed point, we compute $T(\vec{x})$, shown in Panel **E**.

We use the wing image to create a background velocity field where we set the velocity in the darkest pixels to be 1000 times slower than in the lightest pixels. Thus, when the fronts from two different seed points collide, they collide in the vein. This was essential as it allowed us to accurately resolve neighbor information, something that we leverage to convert each domain shape into a polygon. This is helpful for analyzing vein geometry, because a polygon-based representation of vein domains minimizes the effect of pixel-scale noise on the quantitative features of domains.[3] Due to imperfections in the printing process of book images, there are occasionally very small domains that are not seeded accurately. However, when we calculate attributes for all the domains in a wing, we weight values by their constituent domain's area, meaning that these seeding errors have a negligible effect.

1.4   Segmenting other biological images

We show that our segmentation method is effective on a variety of biological images in Fig. S3.

1.5   Assessing the accuracy and consistency of wing images

Since many of the images used in the present study are published wing tracings, we establish that authors of those sources are able to accurately and consistently recapitulate the veins of wings. We do so by comparing our original micrographs to drawings of the wings of the same species in published sources. We also establish that the authors of our published sources do not substantially differ from one another in their drawings of wings.

1.5.1   Comparing between original wing micrographs and published sources

In Fig. S4, we show examples of real wings we captured and imaged directly, compared to wing images of the same species taken from published sources. We find that they are quite similar and that the drawings accurately capture the characteristics of the wings used in this manuscript. For two examples, we show area and circularity maps.

1.5.2   Comparing between wing images from different published sources

In Fig. S5 we compare wings of the same species from two sources. Overall, we find that the two sources agree with one another quite well. In Fig. S6 we compare the size and circularity of domains in a *Dromogomphus spinosus* from both sources.

---

[3]Segmentation imperfections along veins tend to be approximately the same thickness (a few pixels in size). Therefore, the fractional change in properties like area and perimeter is larger for smaller domains. Converting domains to polygons minimizes this effect.
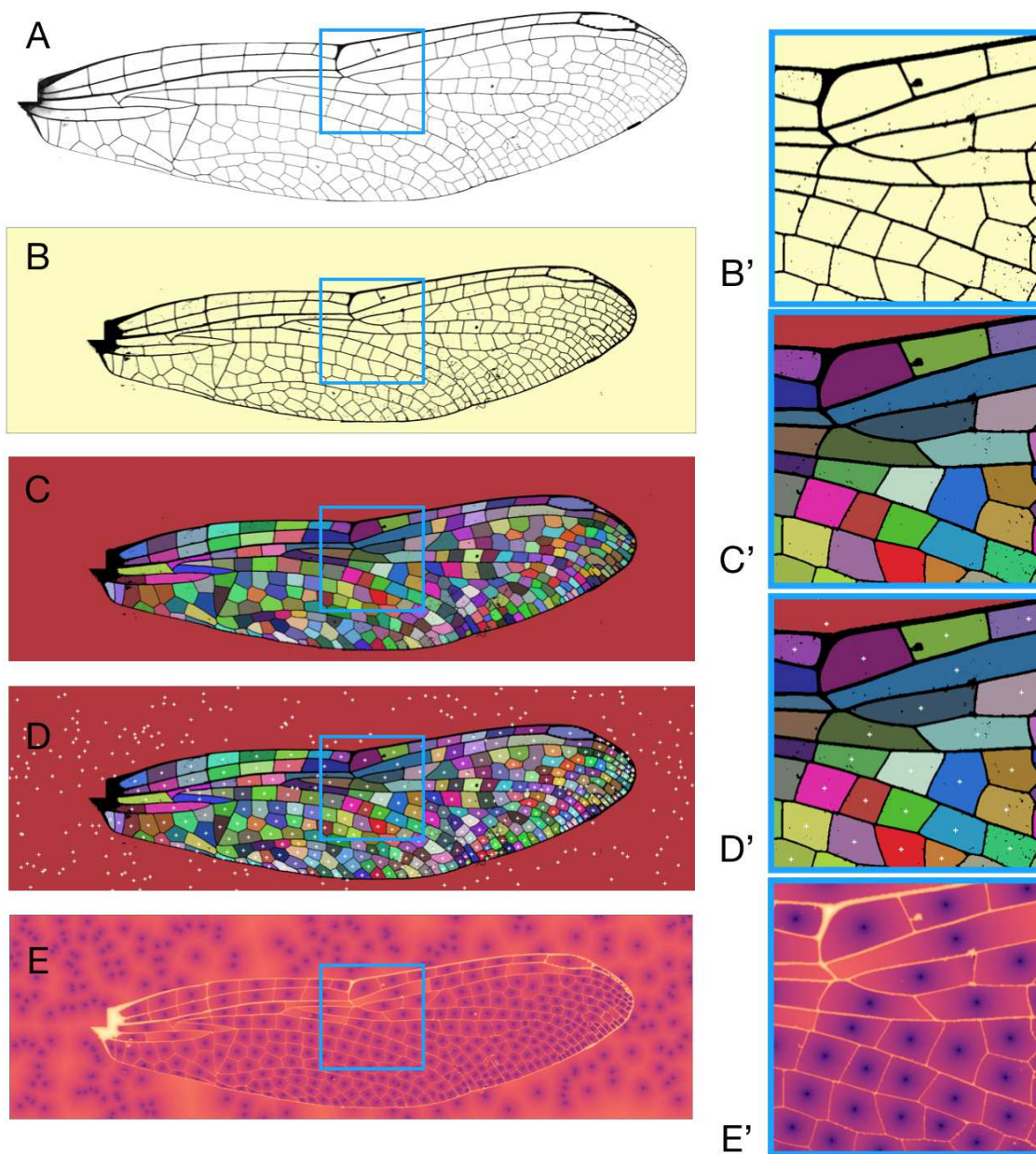
Figure S2: **Segmentation of wing images.** Panel **A** shows the raw image of an insect wing. Panel **B** shows the background velocity field created from the raw wing image. A black pixel has a value of 0.0 and a white pixel to have a value of 1.0. To set the velocity, the formula $v_{i,j} = p_{i,j} + 0.001$ is used, where the offset of 0.001 ensures that the speed through a black vein is 1000 times slower than through free space. Panel **C** shows connected components after thresholding. Points within these components are used as seeds for our fast marching method. Panel **D** shows the seed points from each connected component denoted by a white cross. Panel **E** shows the travel time matrix plotted on a logarithmic scale obtained after solving an equation of the form $F(\vec{x})|\nabla T(\vec{x})| = 1$. $F(\vec{x})$ represents the speed and $T(\vec{x})$ represents the travel time matrix. The figures on the right (**B'**, **C'**, **D'**, **E'**) are magnifications of the regions boxed in blue.
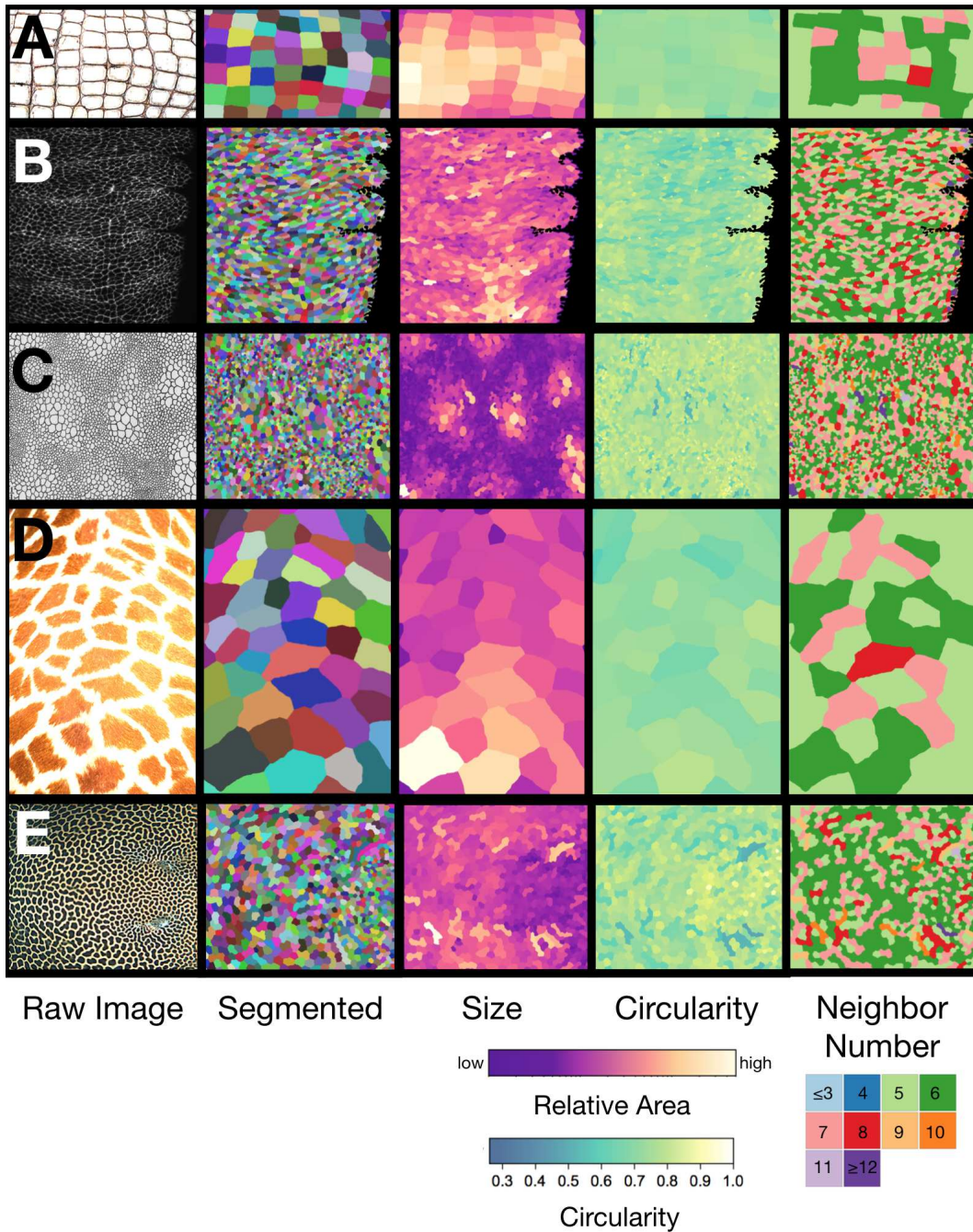
Figure S3: **Segmenting patterns in biology.** Row **A**: Alligator scales. Image courtesy of Matt Eich (photographer) [32]. Row **B**: Developing ventral epidermis on an embryo of *Drosophila melanogaster*. Fixed and stained to show adherens junctions, following immunohistochemistry methods described in Simone and Dinardo (2010) [33]. Row **C**: Abdominal scale imprint of a *Trachodon*. Image courtesy of Wikimedia Commons/Henry Fairfield Osborn [34]. Row **D**: Giraffe Image courtesy of Public Domain Pictures/Petr Kratochvil [35]. Row **E**: Reticulate whipray. Image courtesy of Krystof Tichy (photographer) [36]. First column shows the input image, the second column shows the segmented image with domains colored randomly, the third column shows the relative area of different regions, the fourth column shows the circularity, and the fifth column shows neighbor number.
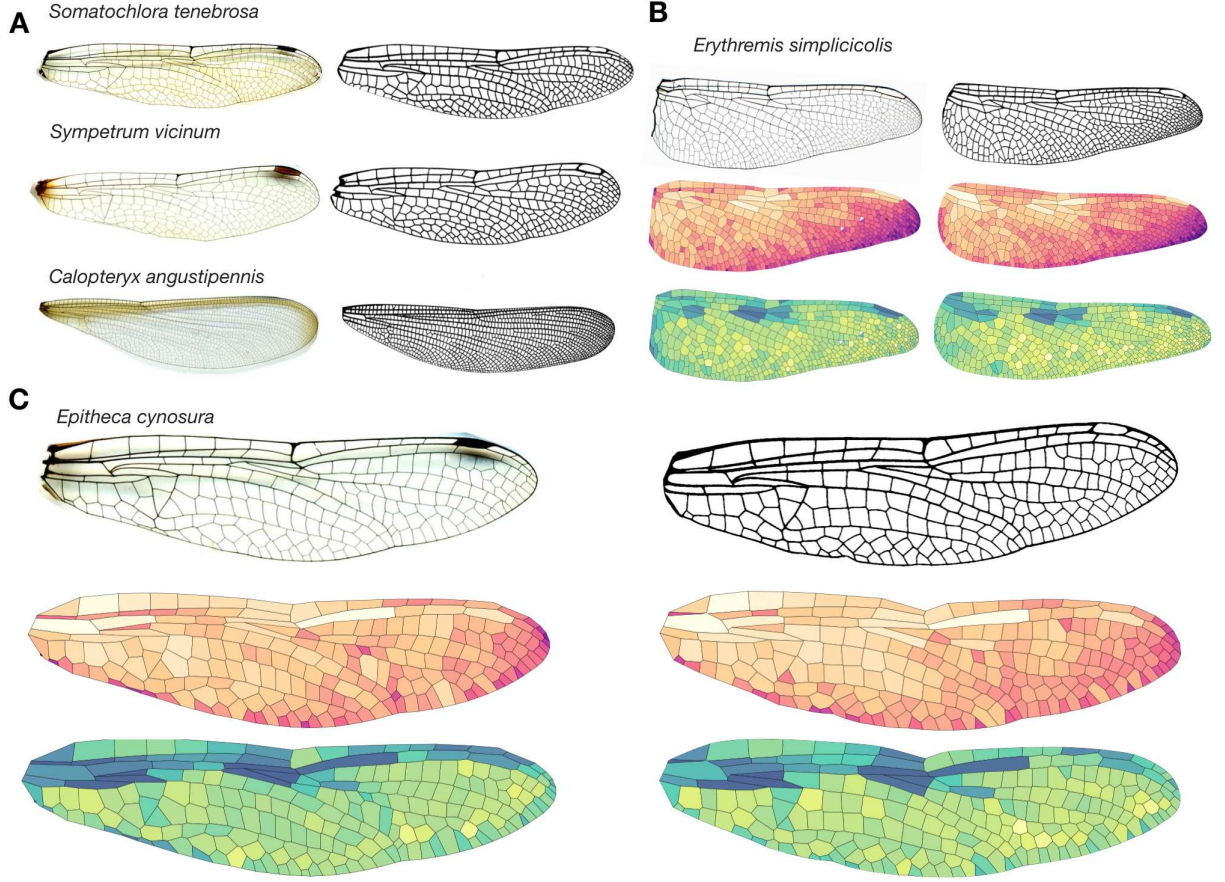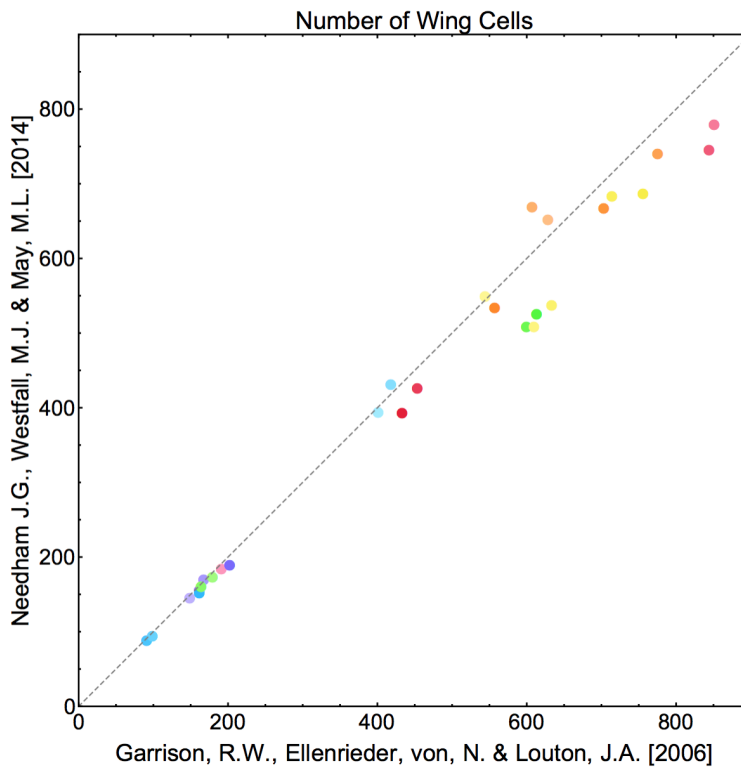
Figure S4: **Comparing original micrographs and published wing images.** Panel **A** shows a series of original dragonfly wing micrographs (on the left) and published images (on the right). Panels **B** and **C** show the segmentation of two different wings, colored by size and circularity, following the color scales in Fig. 1 of the main text. Reprinted with permission from Michael L. May (artist) [1]. From [2], p. 16, Figure 53; p. 97, Figure 587; p. 100, Figure 604; p. 134, Figure 704; p. 157, Figure 864. (c) 2006 Johns Hopkins University Press. Reprinted with permission of Johns Hopkins University Press.

2   Quantitatively characterizing the arrangement of wing veins

2.1   Calculating circularity

For each wing polygon $\mathcal{P}_i$, we compute its circularity by computing the length of its perimeter (∂_i) and its area ($\mathcal{A}(\mathcal{P}_i)$). Defining the radius of a circle with the same perimeter to be $R_c = \partial_i/(2\pi)$, we can then write that the area of the equivalent circle is $A_c = R_c^2 \pi$. The circularity is then given by

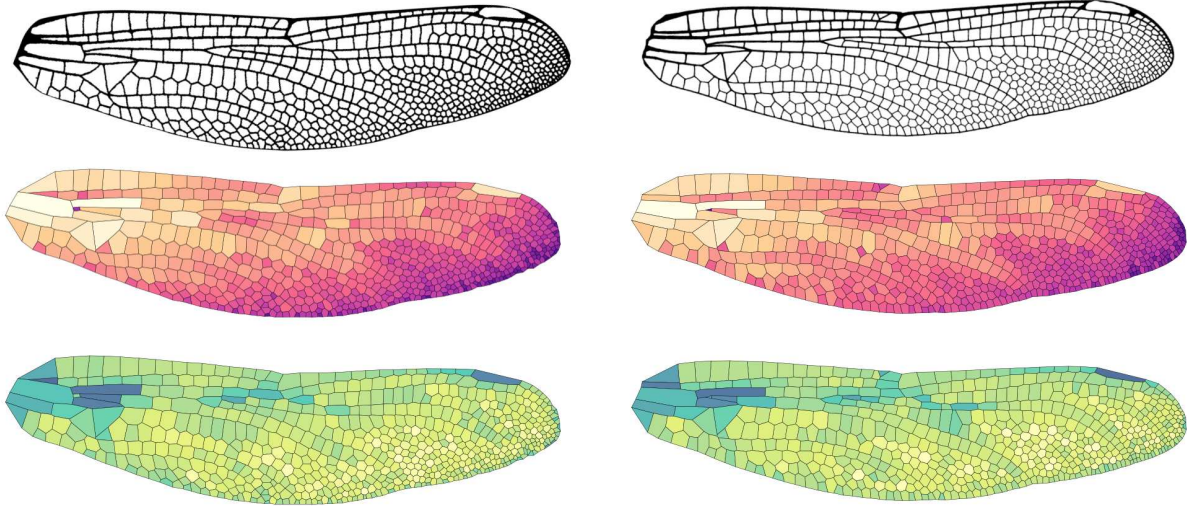$$\mathcal{C}(\mathcal{P}_i) = \frac{\mathcal{A}(\mathcal{P}_i)}{A_c}. \tag{1}$$

Figure S5: **Comparison of wing images from two sources.** Plot showing the number of wing domains that are present in equivalent wings of the same species from the two sources used [1, 2].

Dromogomphus spinosus

Figure S6: **Comparison of a *Dromogomphus spinosus* wing from two sources.** The original wing (top), the wing with domains colored by size (middle), and the wing with domains colored by circularity (bottom). Reprinted with permission from Michael L. May (artist) [1]. From [2], p. 16, Figure 53; p. 97, Figure 587; p. 100, Figure 604; p. 134, Figure 704; p. 157, Figure 864. (c) 2006 Johns Hopkins University Press. Reprinted with permission of Johns Hopkins University Press.

2.2 Vein domain area and circularity for dragonfly and damselfly forewings

In Fig. S7 we show the area and circularity of domains in the smallest, median, and largest dragonfly and damselfly wings.

2.3 Correcting for corrugation

Our original micrographs and the published wing tracings are both two-dimensional projections of wings that have some three-dimensional corrugation [21]. This results in distortion to the observed shapes, illustrated in Fig. S8. Here we attempt to bound the effect of this corrugation on our quantification of domain sizes and shapes. We consider the effect of corrugation slope on fractional area and circularity. We consider "worst case" scenarios, but most of the wing does not have extreme corrugation [21, 22]. In fact, near the tip of the wing, corrugation is nearly absent [22].

2.3.1 The effect of corrugation on area measurements

Let us consider a rectangle with sides of lengths a and b. We can write that $b = \gamma a$ where γ represents the aspect ratio of the rectangle. We observe the rectangle as having $A_o = \gamma a^2$. Suppose that the wing
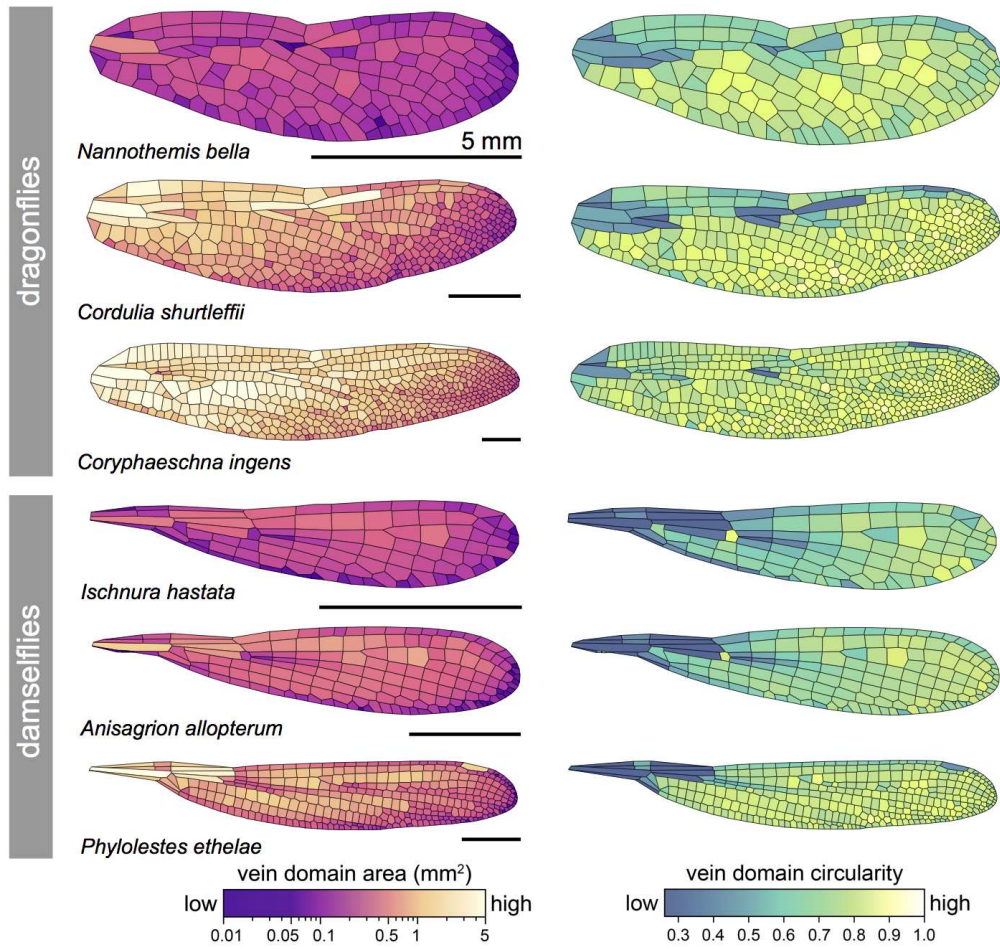
Figure S7: **Dragonfly and damselfly wings with domains colored by area and circularity.** The smallest, median, and largest dragonfly and damselfly wings in our dataset of segmented wings. Scale bar represents 5 mm for all images.

is angled in the direction along the side γa. The true length of this side is then $h = (\gamma a)/\cos(\theta)$. We can write

$$A_t = a\left(\frac{a\gamma}{\cos\theta}\right) \tag{2}$$

as the true area. The ratio of the observed area to the true area is therefore

$$\frac{A_o}{A_t} = \frac{\gamma a^2}{a\left(\frac{a\gamma}{\cos\theta}\right)} = \cos\theta. \tag{3}$$

In Fig. S9 we plot the distortion of area that results as a function of θ. Note that for most domains, the angle is between $0°$ and $5°$. Very few domains lie on corrugations that are angled more than $20°$ (see the profiles in Fig. S9 Panel **B**).
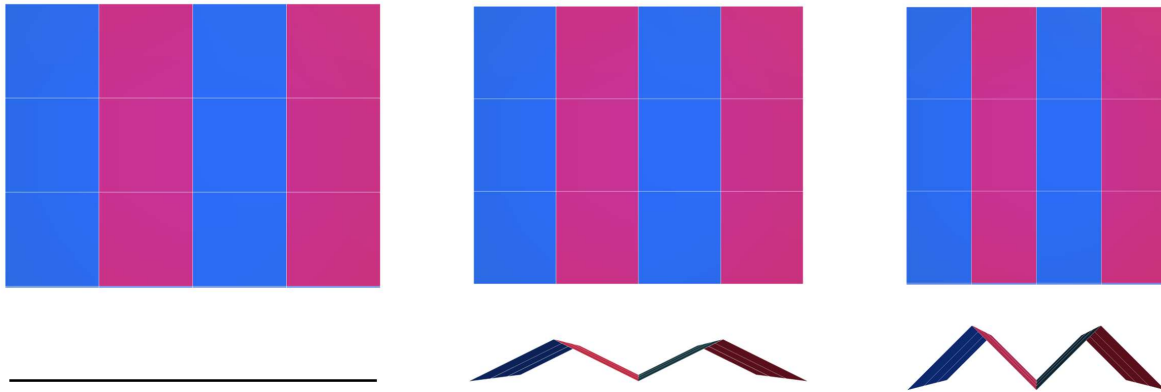
Figure S8: **Corrugation of a wing.** Odonate wings are corrugated. Here we show a top-down projection (**top row**) and side-on view (**bottom row**) of a corrugated sheet. From the top-down views, the squares appear distorted along the axis of corrugation. This distortion is investigated in Figure S9.

2.3.2 The effect of corrugation on circularity measurements

Here we consider how various angles of corrugation would affect the circularity calculation of wing domains that have the shape of a regular triangle, square, pentagon, and hexagon. We also consider the effect on a rectangular domain with aspect ratio 4. In Fig. S10 we show how the circularity of various shapes changes as a function of θ.

We find that for the range of angles that we consider, the effect on circularity is quite small. For the entire range of shapes we observe, deviations of 0–10° of the measured circularity differ from true circularity by less than 1%. Larger deviations in angles only occur in a very limited region of the wing and still result in only minor deviations. The most extreme effect that we see is for a relatively oblong rectangular shape where the change is 11%. For a pentagonal shape, the change is 1.4%.

2.4 Displaying vein domain shape and size features for a single wing

Vein domain shapes and sizes vary across each wing. In an effort to capture this diversity and compare among wings, we plot domain data from whole wings in several different ways. We use wing maps with each domain colored in according to its area or circularity (e.g. Fig. 1B, C in the main text). We also show single-wing scatter plots with each point representing a single domain from a wing, alongside marginal distributions of circularity and area (e.g. Fig. 1C in the main text). We show wings with data grouped by wing region (e.g. Fig. S33). We also plot vein domain features, averaged within bins that span a particularly important biological axis in wings: the proximal-to-distal axis.

2.4.1 Proximal-to-distal morphology traces

The proximal-to-distal (P–D) axis is a well-defined and widely studied axis of insect wings. The P–D axis begins at the hinge where the wing joins the body wall and extends to the farthest tip of the wing. It is
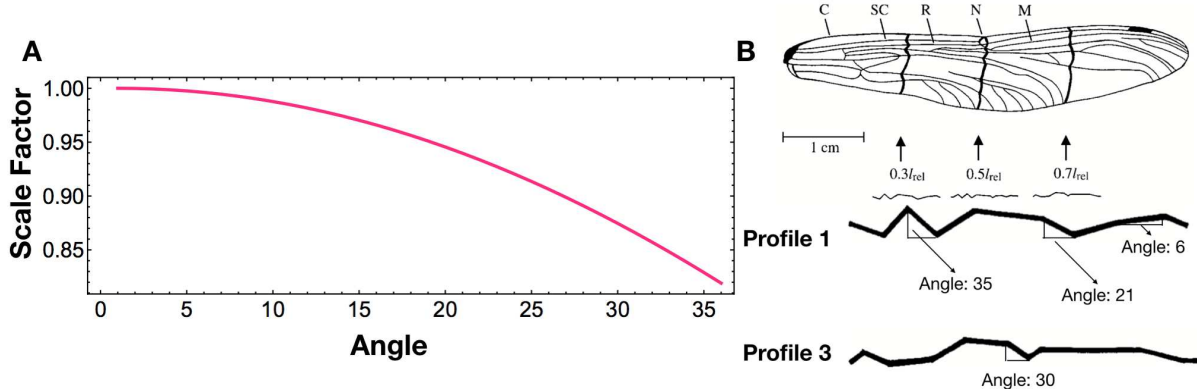
Figure S9: **Effect of corrugation on area.** Panel **A** shows the distortion of area that results from varying its corrugation slope θ for a rectangular object. Note that the curve plotted is merely $\cos(\theta)$. Panel **B** shows cross sections of the wing where the corrugation has been measured. Angles for the most extreme cases have been computed. The 'C', 'SC', 'R', 'N', and 'M' refer to the costa, subcosta, radius, nodus, and mediana primary veins, respectively. Republished with permission of Company of Biologists, from [21]; permission conveyed through Copyright Clearance Center, Inc.

often used as a way to orient morphological or biomechanical attributes of a wing [39, 40, 42, 43]. It has also been identified as a key axis of tissue specification in the wing [38, 41]. In this study we use "P–D wing traces" to summarize how vein domain characteristics vary along the long axis of the wing, which enables us to compare among distantly related insects. It also provides results that can be directly compared to much of the existing morphological, biomechanical, and developmental literature on insect wings. This approach necessarily obscures differences between domains that are in the same position along the P–D axis. Therefore, this is certainly not the only way to summarize vein domain characteristics within a wing. It is nonetheless effective at capturing similarities and differences among insects that are both closely and distantly related. For readers that are interested in comparing species without the dimensional reduction of P–D traces, we have included complete sets of domain attributes for a wing from each odonate species that we study in this paper at http://seas.harvard.edu/~chr/wing_data/.

To construct a P–D wing trace, we represent a wing as a curve through area–circularity space as one moves from the hinge at the wing base to the farthest tip of the wing. To do this, we begin by orienting the wing with the main principal component along the x-axis. We then partition the wing into 21 equal-width rectangular bins along the long axis. We then compute the circularity of each polygonal domain and then compute the area of overlap between the given polygon and the bin we are considering. That is, to calculate the mean circularity of slice i, which we denote $\mathcal{S}_i$, we compute

$$\frac{1}{\sum_{\mathcal{P}_j} \text{Area}(\mathcal{S}_i \cap \mathcal{P}_j)} \sum_{\mathcal{P}_j} \text{Area}\left(\mathcal{S}_i \cap \mathcal{P}_j\right) \mathcal{C}(\mathcal{P}_j) \tag{4}$$

where the sum is taken over all polygons $\mathcal{P}_j$. This produces a smoothly varying mean circularity as we move along the long axis of the wing. For polygon $\mathcal{P}_i$, we obtain the area fraction f_i that overlaps with
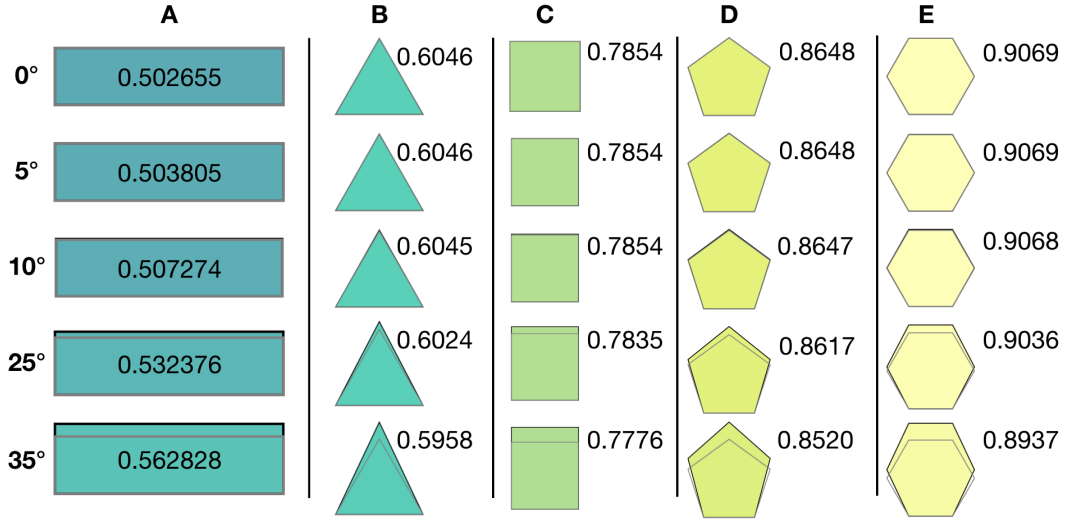
Figure S10: **Effect of corrugation on circularity.** For a series of shapes and angles, the circularity of each polygon is shown. Column **A** shows a rectangle with aspect ratio 4. Columns **B**–**E** show a triangle, square, pentagon, and hexagon. Even for the most extreme corrugation slopes, the error in calculated circularity is quite small.

the bin. We construct the vector of all area fractions in bin i, denoted $\vec{F}_i$. We also have the vector of all circularities $\vec{C}$ and all areas $\vec{A}$. For each bin, we compute

$$(\vec{F}_i \cdot \vec{A}, \vec{F}_i \cdot \vec{C}) \tag{5}$$

giving us the weighted mean area and the mean circularity of the wing domains in the region.

2.5   Comparing forewings and hindwings of the same species

As many workers have observed, forewings and hindwings are more similar to one another in damselflies as compared to dragonflies. In Figure S11, we show the forewing and hindwing of two example dragonflies and damselflies using P–D traces, with images of the wings themselves inset. As expected, the difference between P–D traces of damselfly forewings and hindwings is less than that of dragonflies.

2.6   Intraspecific and intra-individual wing comparisons

Within our dataset, we have 3 sets of *Sympetrum rubicundulum* hindwings. Each hind wing was imaged and segmented to allow us to look at the variation in P–D trace within an individual compared to the variation within a species. In Fig. S12, we show the left/right traces for each individual (Panel **A**) as well as the variation between the different individuals (Panels **B**–**D**). With only three individuals, we cannot conclude that we have effectively captured intraspecific variation, although it is a promising avenue for future work.

In Fig. S13, we show all vein domains in our dataset (over 150,000). Additionally, we show how P–D trajectories vary for the largest and smallest three damselflies and dragonflies in our dataset.

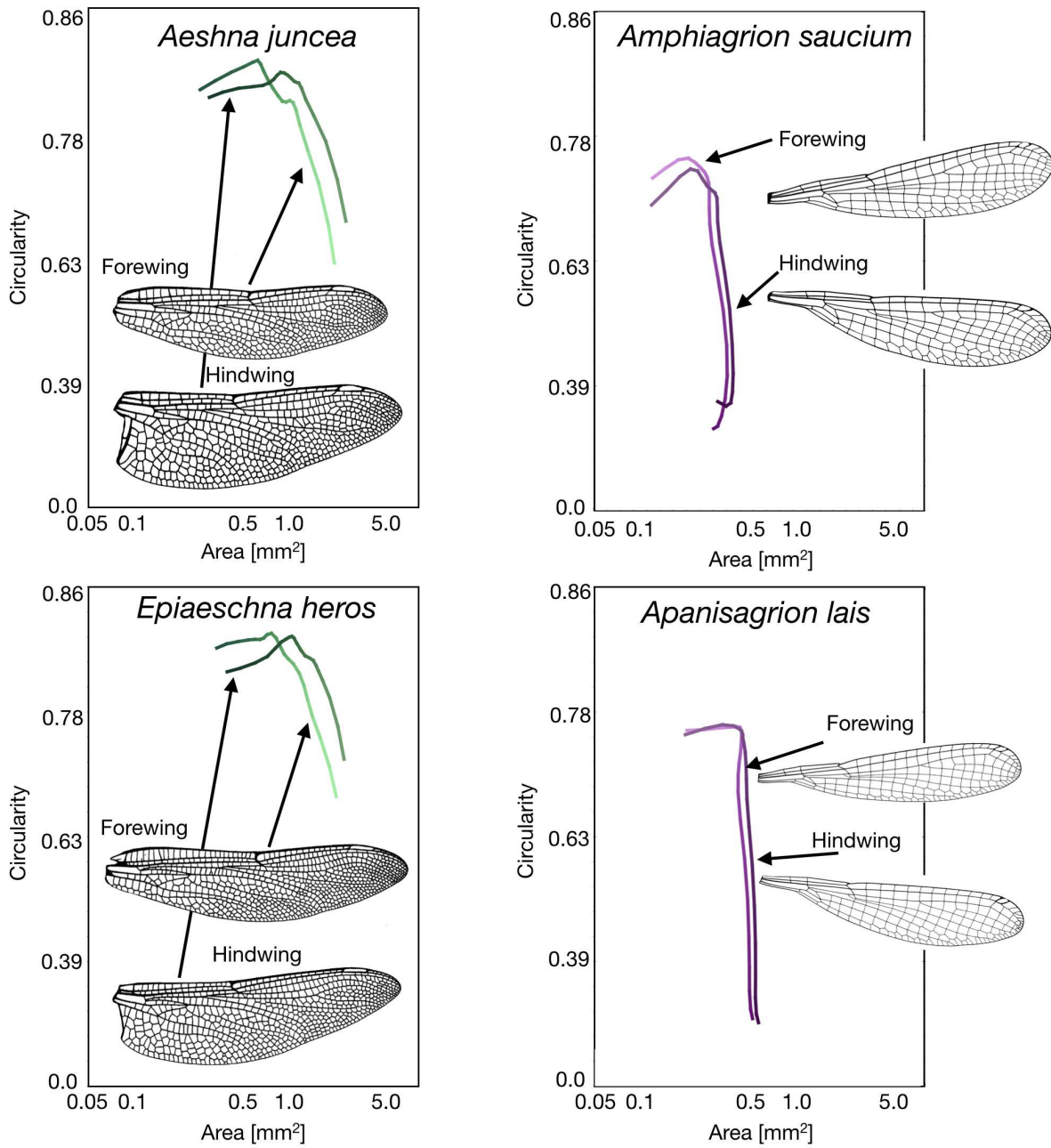Figure S11: **Comparing forewings and hindwings of the same species.** A comparison of the forewing and hindwings of two dragonflies (on the left) and two damselflies (on the right). Reprinted with permission from Michael L. May (artist) [1]. From [2], p. 85, Figure 353; p. 119, Figure 506; p. 196, Figure 1138; p. 209, Figure 1211. (c) 2010 Johns Hopkins University Press. Reprinted with permission of Johns Hopkins University Press.
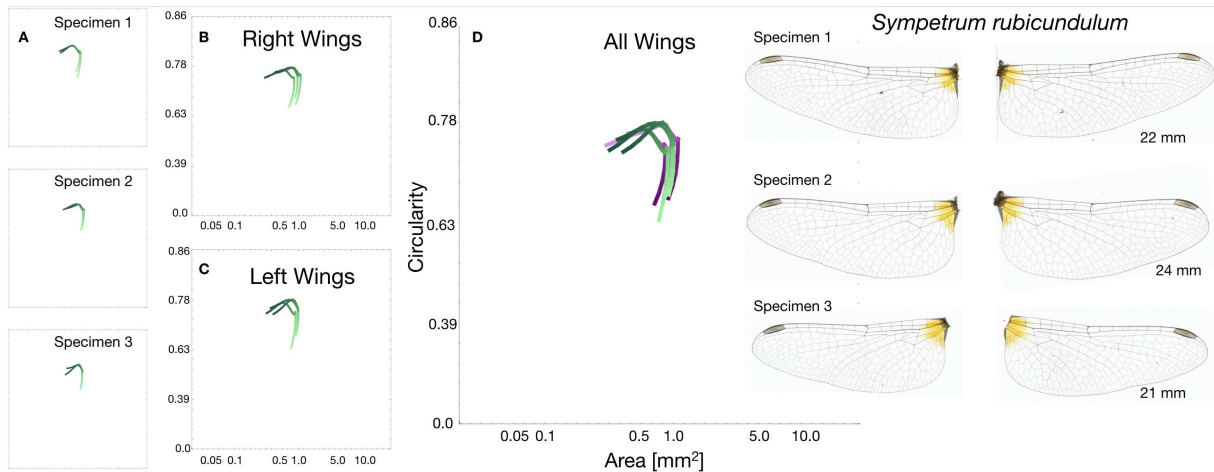
Figure S12: **Variation in P–D traces within individual/species.** Panel **A** shows the P–D traces for the left/right wings of three individuals. In Panels **B–C** just the left/right wings are shown. In Panel **D**, all wings are shown, the left wings in purple. The six wings are shown on the right.

2.7   Domain features of dragonfly in genus *Epiophlebia*

We computed domain features from a drawing of *Epiophlebia superstes*. This genus of dragonfly is of particular interest, as they have the oldest last common ancestor with the rest of the dragonflies. We plotted its P–D trace alongside distributions of traces from dragonflies and damselflies. We used an image from Tillyard [31]. Interestingly, the trace through area–circularity space of the *Epiophlebia* appears to be intermediate between the distributions of damselflies and other dragonflies, as shown in Fig. S14.

2.8   Other quantitative measures of wings

2.8.1   Interior angle distribution

Different regions of the wings are bound by a different number of primary veins. Between two veins that are relatively close together, we typically observe rectilinear domains that form a brick-like pattern. As these long, relatively straight veins diverge, domains have more freedom in forming complex angle distributions. We choose four different wings (two dragonflies and two damselflies) and randomly selected a set of domains bound by zero, one, and two primary veins. For each of these wing domains, we measured all internal angles and in Fig. S15 we show smoothed angular distributions.

2.8.2   Domain sizes in a region

In Fig. S16, we show four wings (two dragonflies and two damselflies) and how each domain's area compares to the mean area of all neighboring domains. We see that there is a very strong positive relationship.
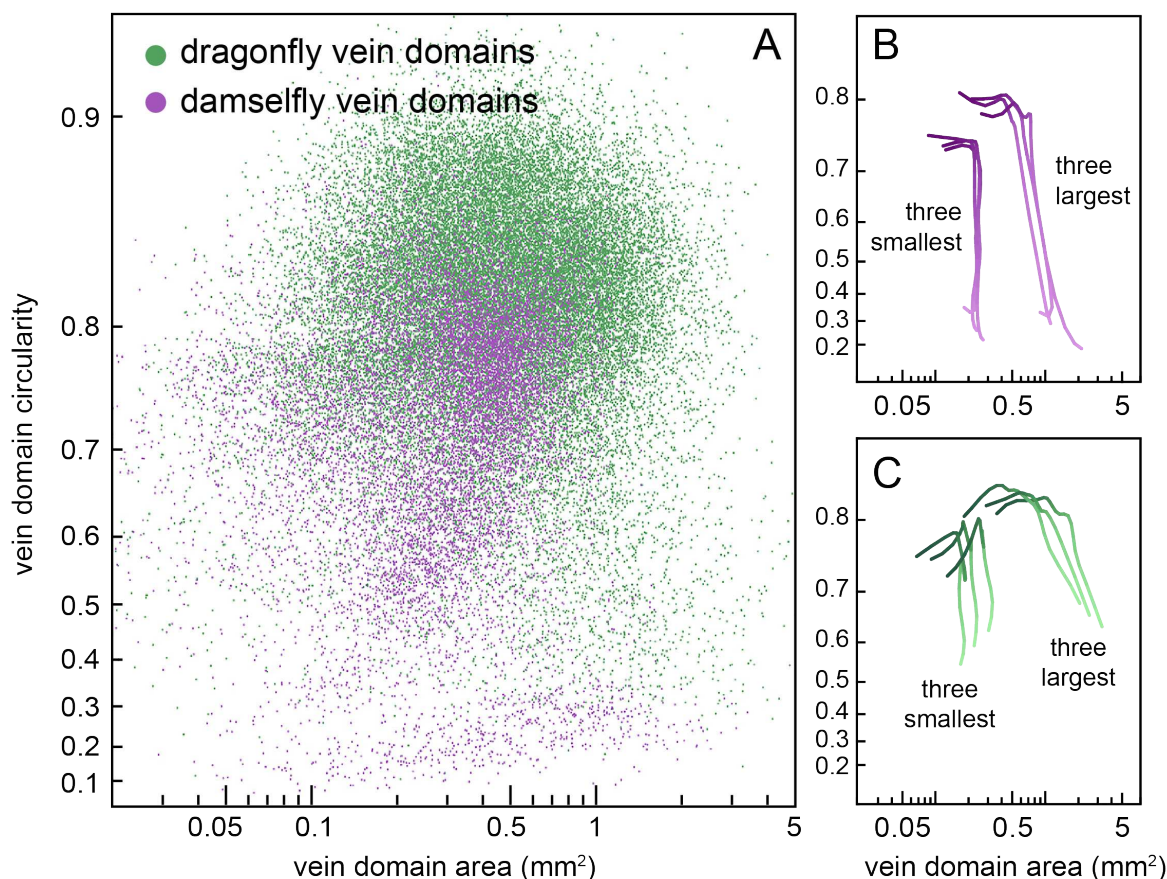
16

Figure S13: **Variation in domains and P–D traces.** Panel **A** shows area versus circularity for all vein domains in our dataset (n > 150,000); dragonflies in green and damselflies in purple. Panels **B, C** show P–D traces of the three largest and three smallest damselflies **B** and dragonflies **C**.

2.8.3 Unconnected vein ends

We observe very few domains that contain incomplete veins. We take a selection of wings imaged directly by the authors and count how many unconnected ends we see in the table below.

2.8.4 Comparison of the number of domains in corresponding regions in left and right wings

In Fig. S17, we count and highlight the number of wing domains in corresponding regions. Shown are the left and right forewing and hindwing from the same individual (*Erythremis simplicicolis*, shown as an example).

3 Procedure for simulating secondary vein patterns

Here we include further details about the vein simulation procedure that is described in the main text and schematized in Fig. 3. Below we have included a subsection for each step of the procedure:
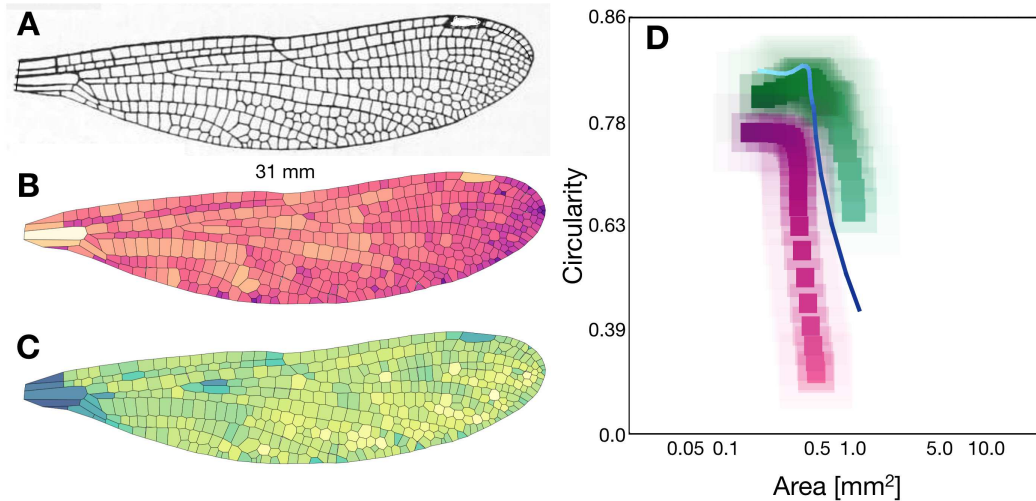
Figure S14: **Wing trace of an *Epiophlebia*.** Panel **A** shows the drawing of a *Epiophlebia superstes* from Tillyard [31]. Panels **B**–**C** show a segmented wing with domains colored by area and circularity. The wing is 31 mm long. Panel **D** shows the curve of the wing (in blue) juxtaposed next to the distributions of wing traces of dragonflies and damselflies.

Aeshna constricta	1
Aeshna verticalis	2
Epitheca cynosura	0
Erythemis simplicicollis	0
Somatochlora tenebrosa	1
Sympetrum rubicundulum	0
Sympetrum vicinum	0

Table 1: Number of unconnected vein ends

- Identifying primary veins for the species we will simulate

- Transforming the adult wing to the shape of its former wing pad

- Seeding inhibitory centers on the wing pad and evenly spacing them using Lloyd's algorithm

- Calculating secondary vein placements as the Voronoi tessellation of the inhibitory centers

- Transforming the wing pad back to the shape of the adult wing

3.1 Identifying primary veins for the species we will simulate

When we simulate secondary veins, primary veins are treated as fixed boundaries within which a stochastic process operates. Thus, the first step of our modeling procedure is to identify the primary veins. We manually identify primary veins, based on three sources of information: (1) overlap among left–right wing pairs, (2) morphological criteria based on published anatomical literature, and (3) conservation of relative positions for consensus vein identifications in the published taxonomic literature. The specific details of this
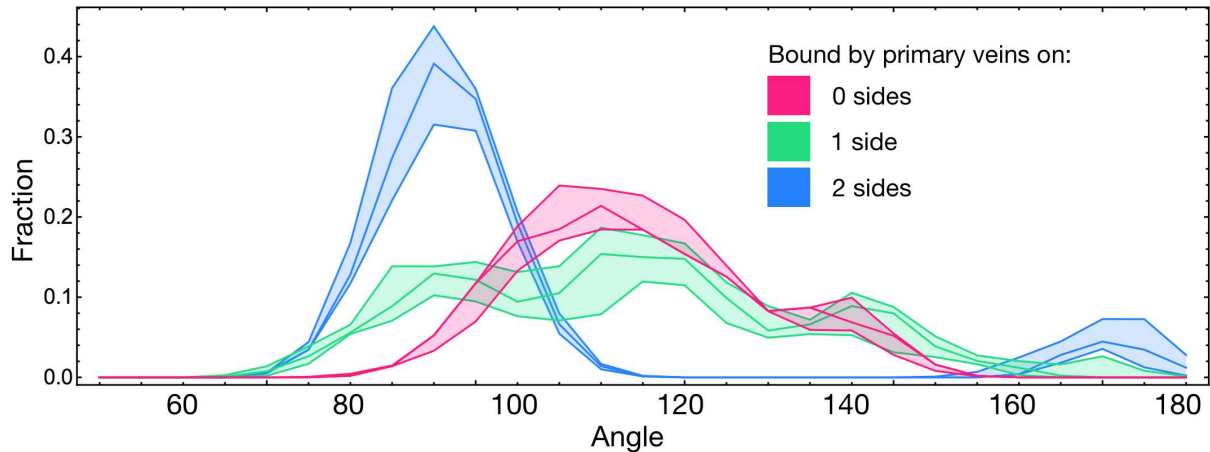
Figure S15: **Interior angle distribution of domains.** Smoothed histograms showing the interior angle distributions of domains bounded by primary veins on zero, one, or two sides (magenta, green, and blue, respectively). Shaded region represents the 1st and 3rd quantiles.

literature-based process for primary vein identification is described in the section below (Section 3.1.1). We then describe two computational alternatives that would allow one to identify primary veins without relying on published anatomical descriptions (Section 3.1.2). We show that these alternatives are not sufficiently effective for the present dataset, but we argue that they should be practical with datasets that include more example wings from a given species. Finally, we show that our technique for simulating secondary veins produces life-like vein patterns even when we vary the primary vein arrangements, demonstrating that our vein simulation results are *not* highly sensitive to primary vein identification (these results are discussed in Section 4.2.2 and shown in Fig. S34).

3.1.1   Literature-based approach for identifying primary veins

As described in the main text, we define a "primary vein" as any wing vein that has a matching counterpart on the opposite wing of the same individual and on the wings of other individuals of the same species. Put more simply: *primary veins are all the veins that are conserved at the species level*.

Thus, the set of primary veins includes long connected segments of veins that are largely collinear, as well as a few conserved cross-veins. Conversely, we define a "secondary vein" as any wing vein that does *not* have a consistently identifiable counterpart on the opposite wing of the same individual and on the wings of other individuals.[4]

---

[4]Naming conventions for insect wing veins has been a matter of considerable debate in the literature because assigning a label to a specific vein is sometimes an act of proposing (or supporting) a hypothesis about evolutionary homology. In this study, we use terms with no intended homology-related implications. For instance, we use "wing vein" to refer to any thickened, strut-like structure in the wing, irrespective of its developmental or evolutionary origin. For the extant taxa included in this paper, the wing veins that we examine also happen to be pigmented and opaque, but we do not consider these traits to be essential attributes of a wing vein. The terms "main vein," "longitudinal vein," "cross-vein," "transverse vein," "fixed vein," and "variable vein"—not to mention "branch," "sector," and numerous taxon-specific terms—have been employed in the literature to refer to subsets of wing veins that may differ from the subsets of veins that we refer to as "primary" and "secondary" veins. For a more comprehensive discussion of wing vein terminology, we refer readers to the many excellent treatments of the topic [3, 4, 5, 6].
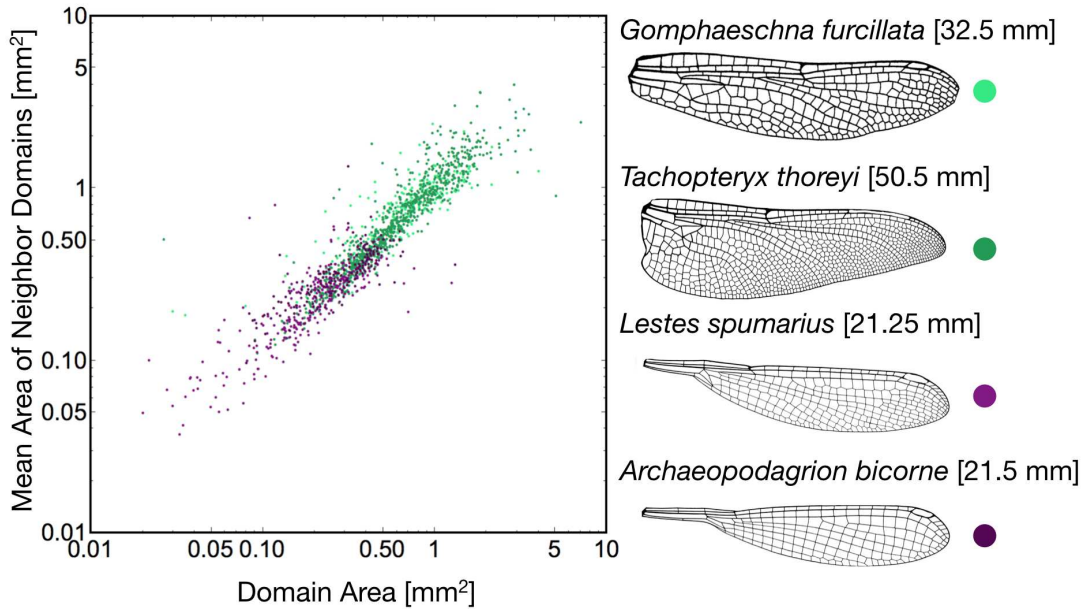
Figure S16: **Domain size compared to mean neighbor domain size.** For each domain in one of four wings, shown on the right, we compute the area of the wing domain. The x-axis shows the area of a given wing domain and the y-axis shows the mean area of all neighboring domains. Reprinted with permission from Michael L. May (artist) [1]. From [2], p. 85, Figure 353; p. 119, Figure 506; p. 196, Figure 1138; p. 209, Figure 1211. (c) 2010 Johns Hopkins University Press. Reprinted with permission of Johns Hopkins University Press.

The simplest way to identify a primary vein is to examine a number of wings from the same species and find the veins whose relative positions can be unambiguously matched across all the wings of that species. Fortunately, that is precisely what entomologists have been doing for over a century. The set of well-conserved veins has been described in many sources [1, 2, 3, 4, 5, 6, 9, 15, 16]. This work has shown that for the majority of primary veins, they are conserved across a wide diversity of species, and even at the level of taxonomic family and order. This previous research has also shown that conserved veins share many morphological features as well: they form the peaks and troughs of wing corrugation [21, 22], often take on a pattern of collinear segments [1, 3, 4, 5, 16], and bear microscopic cuticular structures that are either different from or absent in the rest of the wing [8, 15, 44, 45].

First, we overlap and align the left and right wings from the same individual; see examples in Fig. S25. Then, we manually identify vein placements that are unambiguously shared between the overlapping wings. In cases where veins are close, but not precisely overlapping, we rely on the expertise of previous entomologists to resolve ambiguities. We do so by only identifying a candidate vein as a primary vein if it has the position and/or neighbor collinearity of previously described, well-conserved veins. Finally, we connect all primary veins to form closed shapes by connecting each unconnected end to its closest neighbor.
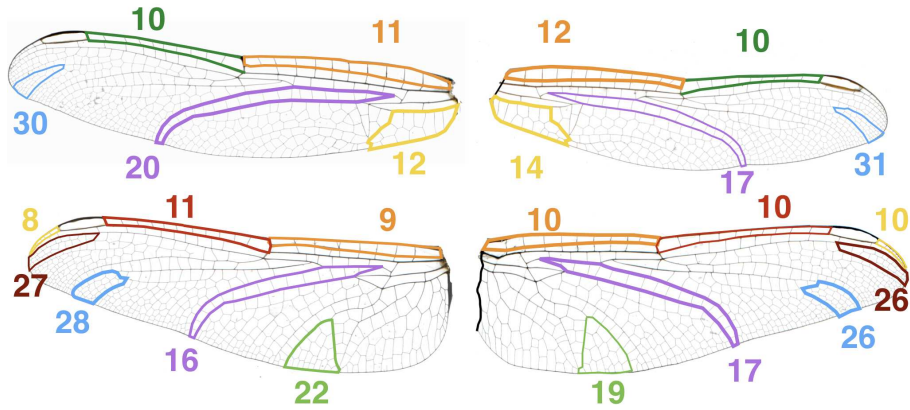
Figure S17: **Number of domains in regions from the left and right wings of a *Erythremis simplicicolis*.** For a selection of regions bounded by primary veins, we show the number vein domains in the corresponding regions of paired wings. Even in the same individual, corresponding wing regions on the left and right wings have a variable number of domains.

3.1.2 Automated approaches for identifying primary veins

Here we discuss two approaches that we have implemented to automatically detect of primary veins. The first method is premised on the fact that primary veins are generally connected to other collinear primary vein segments. Therefore, we score segments based on their collinearity with their neighbors. For this approach, we take one focal vein segment at a time, and for each of its two ends we consider each adjoining vein segment. For each of these, we compute the correlation between the focal vein segment and each of its connected neighbors. We take the maximum value of these correlations at each of the two ends, and discard the smaller values. This results in two correlations. Finally, we compute a "primary vein score" for the focal segment. This is the sum of 0.9 times the larger correlation and 0.1 times the smaller. This weighting scheme was chosen so that intersections that end in a ⊥ do not get discarded. In Figure S18 we show the results of this procedure as applied to the left and right wings of a single individual, wherein vein segments with a "primary vein score" over 0.75 are displayed. In Figure S19 we mirror the left wing onto the right wing to assess whether the veins are shared. We find that when we use this approach on a single left–right pair of wings—but without using any additional additional information from the published literature—we identify long connected primary veins effectively. However, there are also many other scattered, short segments that meet the straightness criterion, but whose positions are rarely shared between the left and right wings. It seems likely that most of these are collinear with their neighbors due to chance alone. If one had access to a larger set of wings, by comparing across more individual wings, one could exclude non-shared segments.

Therefore, we developed an alternative automated approach for identifying primary veins based on correlations of vein segments between multiple wings. After aligning two wings of the same individual, we use a sliding window to calculate the correlation between both wings in a box centered at each pixel. The box side length is allowed to vary across the wing, so that it is always proportional to the local domain
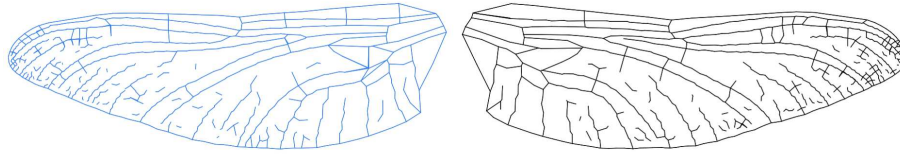
Figure S18: **Vein correlations** Each vein segment has been assigned a "primary vein score" based on its collinearity with its neighbors. Those that have a correlation over a critical value (0.75) are shown in both the left and the right wing (blue and black, respectively).
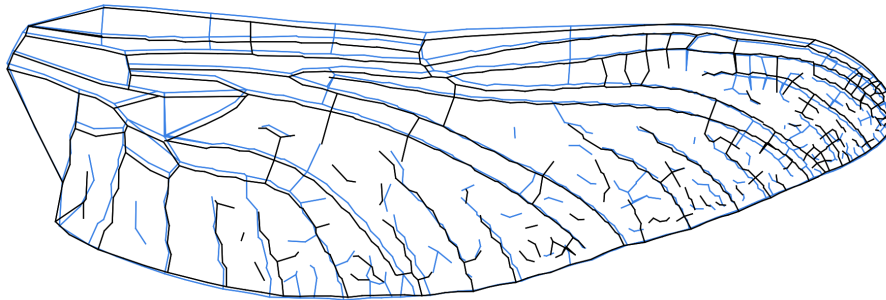

Figure S19: **Vein correlations, aligned.** We flip the left wing onto the right wing where the only veins shown are those that meet a straightness criterion.

size (square root of area). This accounts for the fact that domain size itself varies across the wing. Then, we take the maximum correlation at each pixel and multiply this resulting matrix by a binarized input vein matrix, which gives a correlation value to each vein pixel. These can also be treated as "primary vein scores," assigned at the pixel level. Preliminary results are shown in Figure S20. The result is that veins in an arrangement that is conserved over multiple wings have larger correlation values than those that are not conserved. In the present study we only have one or at most a few wings for each species, so this is not an approach we use for the simulations included in this paper.

Both of these automated approaches require multiple individuals of a given species. In the future, either of these techniques (or perhaps both in combination) could be a promising avenue for high-throughput analysis of even larger wing datasets.

3.2   Transforming the adult wing to the shape of its former wing pad

In Fig. S21, we show the result of our model without properly estimating the shape on the wing pad. Once primary veins have been identified, we estimate the shape of the wing earlier in development—that is, when it was a wing pad and the veins were only beginning to form. The geometry of the wing that we observe is not the same as the geometry of the developing wing. The vein arrangement that formed on the nascent wing pad grows and distorts as the wing itself grows [1, 3, 37].[5] We approximate the effects

---

[5]As described in the main text, we outline the development of wing in broad strokes by supposing that all the primary veins form first, followed by secondary veins. This is almost certainly an oversimplification, but it is suitable for our general
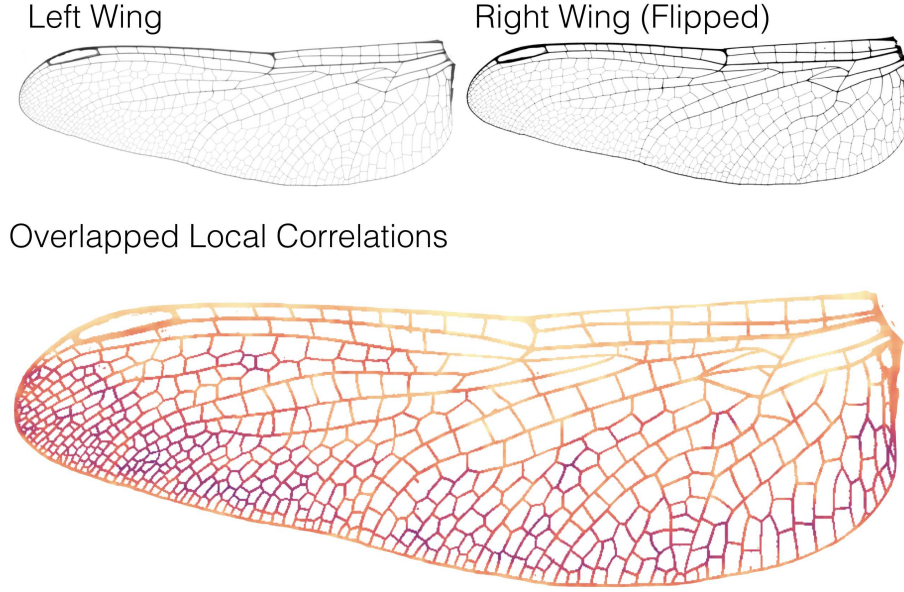
Figure S20: **Local correlation of two wings.** We flip the left wing onto the right wing and determine the local correlation of vein arrangements. Regions with higher correlations are brighter colors than those with smaller correlations.

of this process of anisotropic growth by a process of maximization of the circularity of vein domains.

3.2.1 Remapping a wing to maximize area-weighted circularity of polygonal domains

In our minimal model of vein patterning, we suppose that inhibitory centers emerge stochastically and equilibrate in space, producing a roughly even spacing. These secrete some diffusible signal. Veins form at local minima of this inhibitory signal. Based on this model, the most likely geometry of veins on the wing pad is an arrangement with maximally circular polygonal domain shapes. We consider a transformation that will map a coordinate $(x, y) \rightarrow (x', y')$ where the unprimed coordinates represent what we observe and the primed coordinates are transformed such as that the mean polygon is most circular.

Let us represent an (x, y) coordinate as $\vec{x}$. We write a transformation

$$\vec{x}' = \vec{x} + \sum_{i=0}^{N} \sum_{j=0}^{N} \vec{\alpha}_{i,j} T_i \left(\frac{x}{x_{\max}} \right) T_j \left(\frac{y}{y_{\max}} \right) \tag{6}$$

for some integer N (we use $N = 3$), where we want to find the two-vectors $\vec{\alpha}_{i,j}$ to maximize our objective function. T_i represents the i-th Chebyshev polynomial. When all $\vec{\alpha}_{i,j}$ are $\vec{0}$, we have the identity mapping. We divide by $x_{\max}$ and $y_{\max}$ in x and y to ensure that the x and y coordinates are bounded by -1 and 1.

model. An alternative is that secondary vein inhibitory centers develop after their adjacent primary veins, but before the primary veins have completed their development. We show in the main text that our model can recapitulate secondary vein patterns in Odonata, Orthoptera, and Neuroptera. This suggests that although these distantly related taxa have differing vein ontogenies, they share essential features that are consistent with the assumptions of our model. See [3, 37] for a more detailed discussion of the development of diverse insect wing veins.
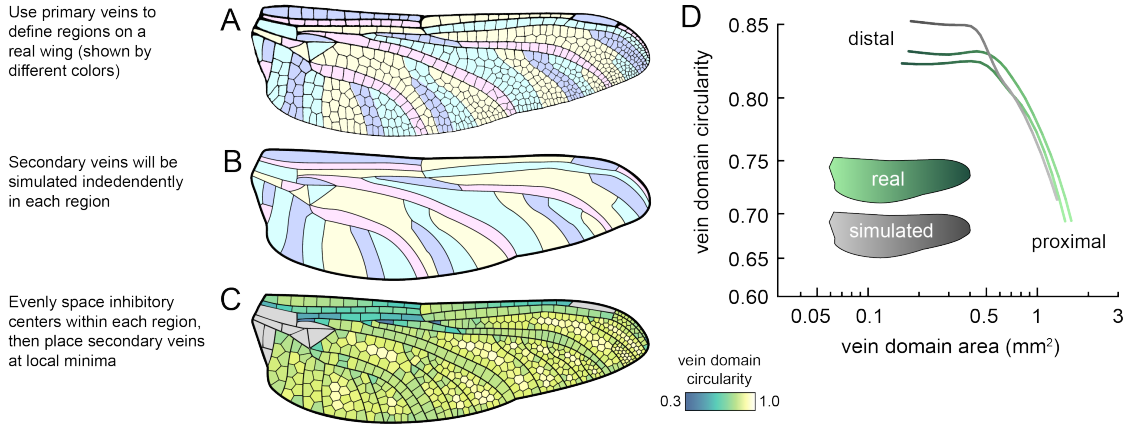
Figure S21: **A model for simulating secondary vein patterning.** Panels **A**-**C** show a process for simulating secondary veins without taking tissue growth into account (*D. spinosus* shown as an example). Gray domains in **C** are bounded on all sides by primary wing veins; these are not simulated in the model. Panel **D** shows P–D morphology traces for the simulated wing and a left-right pair of real wings.

To compute the $\vec{\alpha}_{i,j}$, we want to maximize the area-weighted circularity, where we weight the circularity of each domain by its original area. However, in order to keep the resulting wing pad shapes consistent with examples in the biological literature (see references 34, 36, 38, 39, 40, 41, and 42 in the main text for examples), we impose the constraint that the resulting shape be convex. Since the wings are generally long and thin, we found that maximizing area-weighted circularity alone would lead to a poorly constrained degree of freedom corresponding to a bending mode along the proximal-to-distal axis. Requiring that the shapes be convex is therefore a biologically reasonable way to fully constrain the maximization problem. To penalize shapes that are not convex, we multiply the circularity term by a factor γ that we define to be

$$\gamma = \frac{\sum_i \text{Area}_{\text{transformed}}(\mathcal{P}_i)}{\text{Area}(\text{Convex Hull})}. \tag{7}$$

In the above equation we define the convex hull to be that of the entire wing. In Figure S22, we investigate how different methods of including the γ term affect the resulting shape. When the term is omitted, the bending mode along the P–D axis is visible. We choose to use a linear term, but find that the specific exponent of γ has negligible effect on the wing pad shape that results. For our optimization routine, we want to find

$$\max \gamma \sum_i \left(\text{Area}_{\text{orig}}(\mathcal{P}_i) \text{Circ}_{\text{trans}}(\mathcal{P}_i) \right). \tag{8}$$

In the expression above, $\text{Area}_{\text{orig}}(\mathcal{P}_i)$ represents the original area of polygon $\mathcal{P}_i$ and $\text{Circ}_{\text{trans}}(\mathcal{P}_i)$ represents the circularity of the transformed polygon $\mathcal{P}_i$. While we can no longer easily differentiate this quantity, by artificially perturbing each component of the $\vec{\alpha}_{i,j}$ we are able to estimate the derivative. We use our numerically computed gradients for the Broyden–Fletcher–Goldfarb–Shanno (BFGS) optimization method [29].

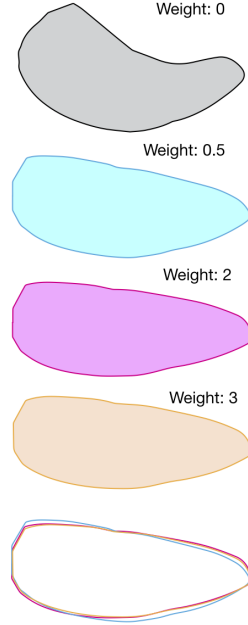|	
γ	Area divided by that of convex hull
$\text{Area}_{\text{orig}}(\mathcal{P}_i)$	Original Area of Polygon i
$\text{Circ}_{\text{trans}}(\mathcal{P}_i)$	Circularity of Transformed Polygon i

Figure S22: **The effect of gamma.** We define γ to be the ratio of the total area of the wing domains to the convex hull enclosing the wing domains. In our optimization routine we incorporate a multiplicative factor of γ^1 into our objective function. Without a γ (or equivalently, with γ^0), we get shapes that are not biologically realistic. In this figure we show γ^0 on top, $\gamma^{0.5}$ second from the top, γ^2 in the middle, and γ^3 second from the bottom. On the bottom, we overlay the final three shapes. We find they are all quite similar and the choice of exponent is not crucial for our analysis.

3.2.2 Comparing circularity maximization to biological data

In order to assess the accuracy of our circularity maximization routine for estimated wing pad shape, we use an example published wing pad for hindwing of a developing *Anax junius* [1]. A tracing of the wing pad is shown in Figure S23. Many primary veins are visible on the pad, with the identities of specific wing morphologies indicated by the author. We begin by tracing primary veins that are identifiable on both the wing pad and the adult wing. Next, we randomly select 15,000 pixels that belong to veins from both the observed wing and the image of the wing on the wing pad. To compute the mapping, we write a transformation of the form in Equation 6. We denote points within the veins of the wing pad as p_i and points in the (transformed) observed wing as q_j. We can then write the cost function as

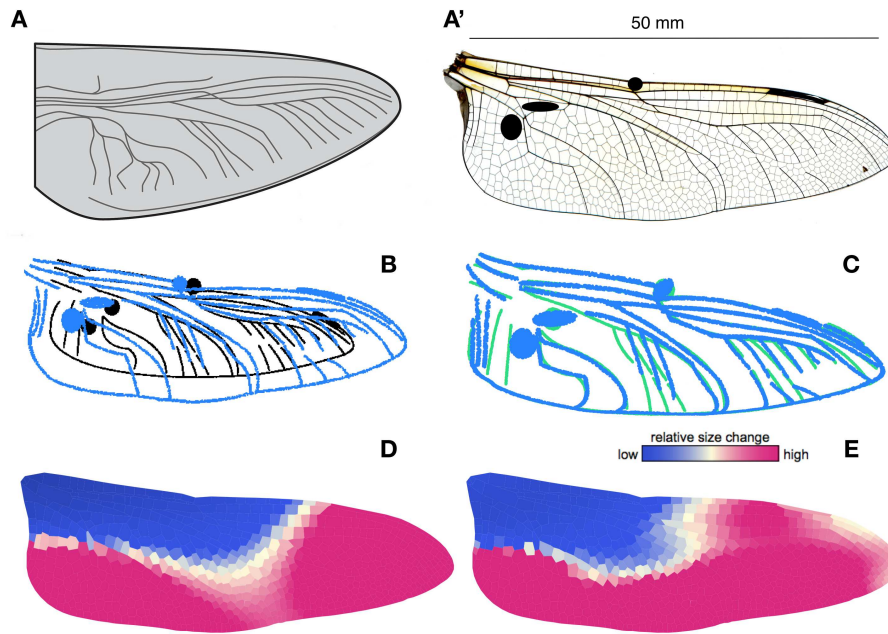$$\text{cost} = \sum_i \min_j(d(p_i, q_j)) + \sum_j \min_i(d(q_j, p_i)). \tag{9}$$

Figure S23: **Comparing circularity maximization with landmark-based growth of the wing pad.** Panel **A** shows the developing wing pad of (*Anax junius*), as adapted from [1]. Panel **A'** shows a wing image of an adult from the same species. The adult wing is 50 mm long. Corresponding vein regions are marked in black. Panel **B** shows the wing veins we marked in **A'** in blue along with landmarks identified from the wing pad in black. Panel **C** shows the result after using the landmarks to map the wing pad onto the adult wing. The transformed wing pad landmarks are shown in green. Panel **D** shows the relative local growth in the wing pad, mapped onto the adult wing, as estimated via the circularity maximization routine described in the text. The colormap represents the estimated relative local growth of the wing. Blue domains are estimated to grow the least, while magenta grows the most. Panel **E** shows the relative local growth of the wing, as estimated from landmarks on the wing pad and the adult wing. Scale bar in Panel **A'** applies to Panel **D** and **E**. Panels **B** and **C** are unscaled. The original source for Panel **A** [1] did not include scale information; given that we are estimating *relative* growth, the absolute scale is not needed.

We include two symmetric terms such that we minimize the distance between points from the transformed wing to the wing pad and from the wing pad to the transformed wing (this ensures that all points are not collapsed in space). The procedure and its results are outlined in Fig. S23, Panels A–C.

We assess the accuracy of our circularity maximization routine for estimating the wing pad by comparing the wing-to-pad transformation for the estimated wing to the transformation for the true wing. For each wing domain, we compute the fractional area before and after the deformation. The results are shown in Fig. S23 Panel D. On the whole, we found that our circularity maximization routine broadly captures patterns of anisotropic growth of the wing. Specifically, we find that base of the wing grows relatively less that the rest of the wing during development, while other parts of the wing get relatively larger; this pattern is recapitulated with the circularity maximization routine.

3.3 Seeding inhibitory centers on the wing pad and evenly spacing them using Lloyd's algorithm

To equilibrate seed points in space, we use an algorithm known as Lloyd's algorithm or Voronoi Iteration [30]. A Voronoi cell is defined to be the region around a seed point that is closer to the seed than to any other seed. Lloyd's algorithm proceeds by iteratively moving all seeds to the centroid of their Voronoi cell.
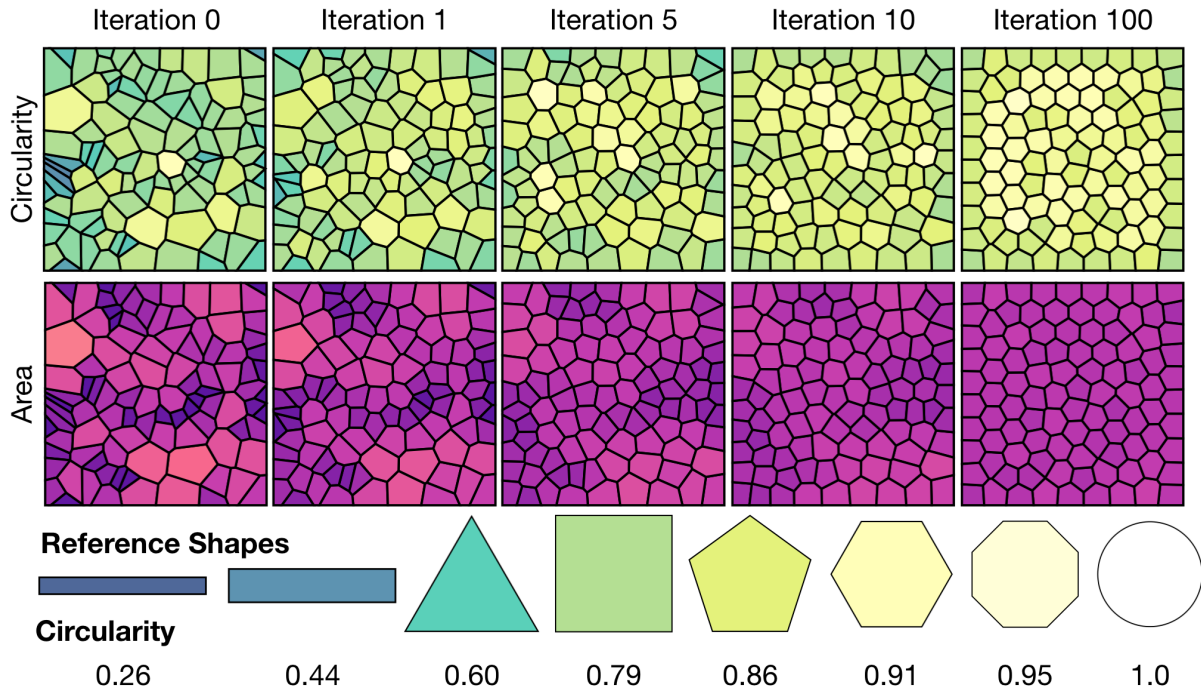

Figure S24: **Iterations of Lloyd's algorithm.** The random initial configuration (iteration 0), and iterations 1, 5, 10 and 100 of Lloyd's algorithm. At each iteration, domains are colored by circularity (top row) and size (middle row). The bottom row shows various reference shapes colored by their circularity.

Figure S24 shows several iterations of Lloyd's algorithm. A random collection of points equilibrate into an equally spaced lattice. Note that the geometry of domains around the boundary are different from those in the interior.

In the transformed wing, we drop a number of seed points into each primary vein bound region. The number of seeds is either determined empirically from real wings (main text, Figs. 3–4) or estimated from the local thickness of primary veins (main text, Fig. 5); we discuss this further in the next section. We find that the initial spatial distribution of seeds in each region does not matter at all. After iterating their position through Lloyd's algorithm, they equilibrate to indistinguishable distributions. The number of required iterations varied depending on wing size and number of domains. We terminated Lloyd's algorithm once the mean change in seed positions dropped below 0.1% of the length of the wing.[6] After updating the locations of all points, we remap the distorted wing back to the untransformed wing geometry.

---

[6]Typically, we ran between 100 and 1000 iterations to reach the endpoint.
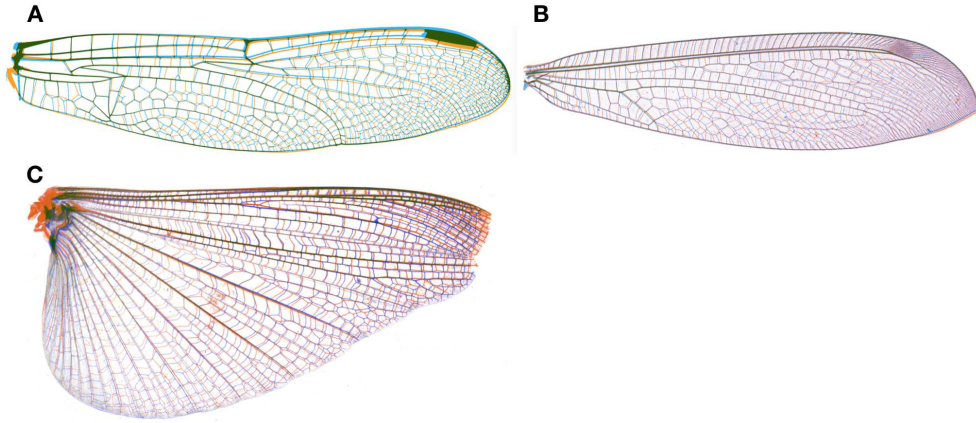
Figure S25: **Overlaying left/right wings of the same individual.** Panel **A**: Dragonfly, Panel **B**: Neuroptera, Panel **C**: Orthoptera.

3.3.1 Determining the number seed points in each region

As described in the main text, we use two approaches to determine the number of inhibitory centers that we seed into regions bound by primary veins: (1) we use the empirical count of domains in each region in the true wing (shown in main text Fig. 3); (2) we use information based on the thickness of surrounding primary veins (shown in main text Fig. 5). The latter approach is described in the main text and in further detail in this section.

Near larger domains, primary veins are thicker; near smaller domains, primary veins are thinner (see main text Fig. 5, and additional information below in Section 3.3.2). We hypothesized that the primary veins on the wing pad are the source of a morphogen whose concentration determines the local length scale of the pattern generator. If so, one might expect that the thickness of the primary veins would be positively related to the strength of the secreted signal. There is little data available on the morphology of primary veins on the wing pad, but in one example case, we find that the thicknesses of primary veins on the wing pad are correlated with their thicknesses on the adult wing (Fig. S26). Therefore, we use adult vein thickness as a proxy for wing pad vein thickness hereafter.

For three different species for which we had original wing micrographs, we used `Fiji` to manually measure the primary vein thicknesses in pixels (the measured primary veins from an example wing are shown in Fig. S27 Panel A) across the wing. Then, for each wing domain centroid we compute the distance to each primary vein. We take a weighted average of primary vein thickness, where we weight each thickness by

$$\text{weight} = \exp\left(-\frac{r}{0.515663 \text{ mm}}\right) \tag{10}$$

where r is the distance from the centroid of the domain in consideration to the closest point on the primary vein. We also introduce a scale factor to convert the pixel value to a width in mm. This results in a locally weighted "primary vein thickness" (in mm) for each domain (Fig. S27 Panel B). We emphasize that the exponential decay function in Eq. (10) is a modeling assumption, and that other functional
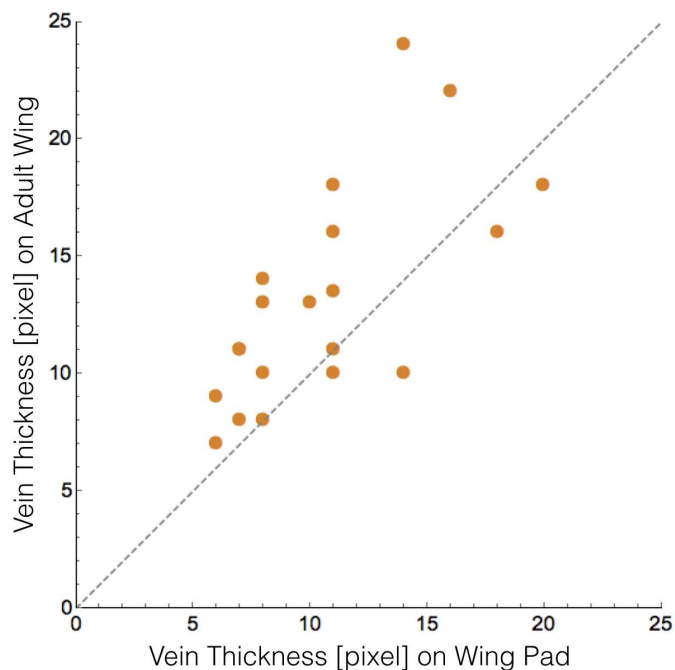
Figure S26: **Vein thickness correlates between wing pad and adult wing.** Various non ambiguous vein thicknesses were manually measured in `ImageJ/Fiji` on the wing pad and on the adult wing. Pixel values were rescaled so the wings were the same size. The correlation coefficient is 0.7246.

forms, such as a Gaussian decay, $\exp(-r^2/L^2)$ could be used. We suggest that an exponential decay is a reasonable choice, since it is the steady-state solution for a signal that is diffusing from a vein and decaying with a constant rate. We expect that our results are insensitive to the precise choice of this decay, but this could be investigated further in future work. The pooled data from three example species is shown in Fig. S27 Panel C.

We use the empirical relationship between primary vein thickness and domain size (Fig. S27 Panel C) to determine the number of inhibitory seeds in each wing region for a species that was *not* included in our initial dataset of primary vein thicknesses. We measure the primary vein thicknesses of the new wing, and then randomly draw domains from the thickness distribution shown in Fig. S27 Panel C until the cumulative domain area exceeds the true area of the region. This results in a simulated wing venation pattern whose circularity-area P–D trace is shown in gray in Fig. S27 Panel D, compared to the true left and right wing traces shown in green.

We also evaluated the sensitivity of our simulation results to the number of inhibitory seeds, finding that varying the number of seeds in a region alters the local domain geometries (Fig. S27 Panel D). With too many seeds, domains are both smaller and more circular than the true wing. With too few seeds, domains tend to be larger and more rectangular. To assess this sensitivity, and the relative success of our model, we perform simulations where we seed each region with 0.5, 0.75, 1.25, and 1.5 as many seed points as are found in the real wing (Fig. S27 Panel D).
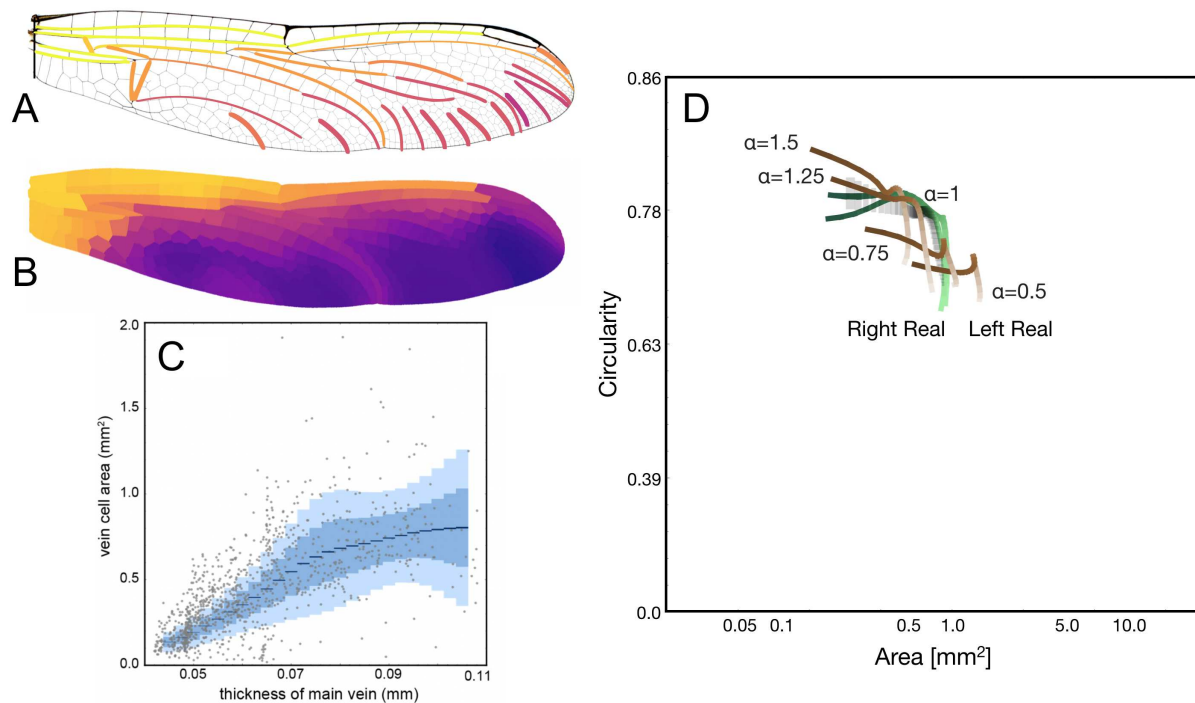
Figure S27: **Primary vein thickness correlates with nearby domain sizes.** Panel **A** shows the primary vein segments used colored by their thickness. Panel **B** shows weighted local primary vein thickness (in mm) for each domain. In Panel **C** we plot vein thickness against domain area for all domains. Panel **D** shows the P–D trace distribution of simulations of a new wing, with seed number determined solely by measuring primary vein thickness and drawing from the distribution of thicknesses and domain areas **C**. The results are shown in gray. The two green curves represent the true left and right wings of the simulated species. We also assessed the sensitivity of the simulation to inhibitory seed number by purposefully overseeding/underseeding regions by scale factors ranging from 0.5 to 1.5. Wing traces from those simulations are shown in brown.

3.3.2   Scaling of vein thickness and domain size across species

As described above, there is a positive relationship between the size of a domain and the thickness of nearby primary veins. To see the extent of this relationship across species, we use a selection of wing images and follow the procedure described in Section 3.3.1. Results are shown in Fig. S28. We find that subtle differences in illumination can affect the measured vein thickness in a wing-specific manner. Therefore we shift all profiles towards the origin by subtracting the smallest vein thickness among all measured veins on that wing. We then fit the relationship between domain size and vein thickness in all wings using an equation of the form domain size $= a(\text{vein thickness})^b$. We report a 90% confidence interval on a and b for each fit.

3.4   Calculating secondary vein placements as the Voronoi tessellation of the inhibitory centers

As described above, a Voronoi tessellation is defined to be the region around a seed point that is closer to the seed point than to any other point. Many features of odonate wing domains are qualitatively similar
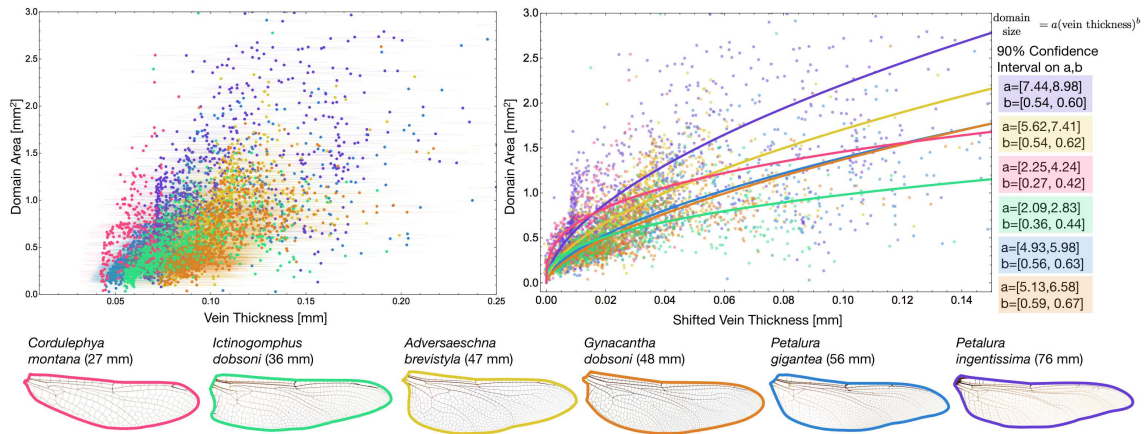
Figure S28: **Scaling of vein thickness with domain size.** Left panel shows the scaling of vein thickness and domain size for six wings (outlined in corresponding colors underneath). Error bars represent a measurement error of one pixel. To minimize the effect of illumination on measured thickness, we shift all points towards the origin before fitting (right panel). Fits are of the form a(vein thickness)^b. 90% confidence intervals of the parameters are given. Wing images courtesy of Wikimedia Commons/John Tann [23, 24, 25, 26, 27, 28].

to shapes that can result from a Voronoi tessellation around equilibrated points. For example, domains in large regions are mostly hexagonal or pentagonal shapes while those in more confined regions tend to be more rectilinear shapes (see the angle distribution in Fig. S15), and cells tend to be similar sizes to their neighbors (see Fig. S16). In Fig. S29, we show various shapes that result from a Voronoi tessellation of evenly spaced seeds.

Our simplified model of secondary vein development is premised on the idea that an inhibitory signal emanates from seeds whose positions are equilibrated in space. In simulating secondary vein geometries on the wing pad, we simply take the equilibrated seed locations in each region and calculate the Voronoi tessellation to simulate the secondary veins.

3.5 Transforming the wing pad back to the shape of the adult wing

Once the secondary veins have been calculated on the estimated wing pad, we reverse the transformation described in Section 3.2 to recover the shape of the adult wing. As described above in Section 3.2.2, we find that our procedure for estimating the growth of the wing pad effectively recapitulates an example wing pad from the literature.

4 Simulation results

4.1 Modeling a damselfly

In the main text we demonstrate simulated venation for a dragonfly, grasshopper, and lacewing. Here, we also apply the same code to model a damselfly, *Hypolestes clara*. Results are shown in Fig. S30.
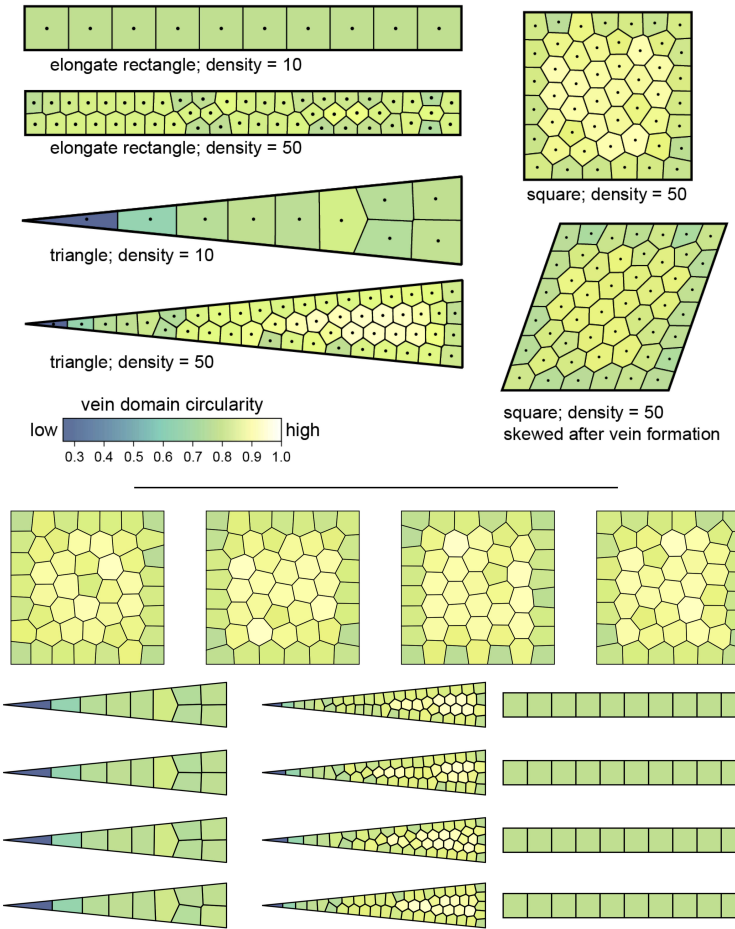
Figure S29: **Example Voronoi Shapes.** In various geometries and densities, the Voronoi cells of equilibrated points are shown, colored by circularity. For the case of a square, we show how circularities transform under a shear. The bottom panel shows near-equilibrated distributions for four runs of different biologically reasonable geometries and densities.
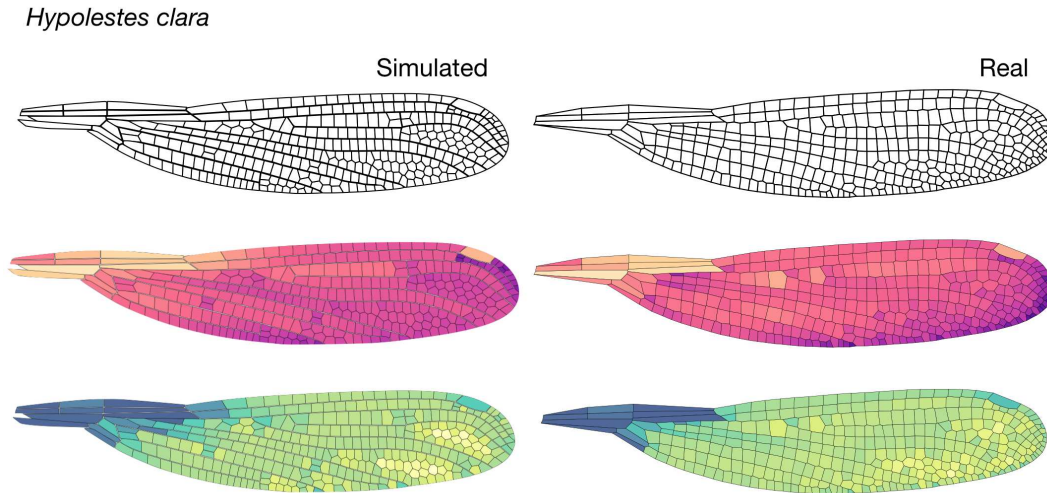
Hypolestes clara

Simulated   Real

Figure S30: **Modeling *Hypolestes clara*.** The model applied to the wing of *Hypolestes clara*.

4.2 Accuracy of vein simulations

4.2.1 Absolute and relative error of vein simulations

In Fig. S32, we compute the relative error in circularity and area between the real vein pattern and our simulated vein pattern for an example dragonfly and damselfly. In Fig. S32, we show the relative error. To calculate these error values, we begin by finding the length of the longest axis, L. We also subdivide each polygonal domain into many small triangles. Each triangle vertex is assigned the area and circularity of the polygon it comes from. We then smooth an area map and a circularity map over the entire wing, where we use a weight proportional to $\exp(-d_{ij}/(0.025L))$ where d_{ij} represents the distance between vertices i and j. Consistent with the results from our P–D wing traces, we see that we underestimate the size of wing domains near the trailing edge of the wing in both dragonflies and damselflies. As a result, we slightly overestimate the area near the leading edge of the wing. It is worth noting that our largest error in the dragonfly comes from a mismatch for just the largest single wing domain in the dragonfly at the base of the wing.

We also assess the error of the simulation in each of the regions bound by primary veins. In Fig. S33 we show the relative error in each region between a simulated dragonfly and damselfly. Domains that are bound by primary veins on all sides are shown in gray.

4.2.2 Sensitivity of primary vein selection on simulated vein patterns

There is broad consensus on which veins are conserved (that is, which ones are primary veins), but there are probably a few of cases in which the published literature includes errors in identifying veins—e.g. secondary veins erroneously identified as primary veins—and vice versa. It is also possible that a simple dichotomy of primary and secondary veins does not fully describe all veins on all species. Therefore, we do not assume that our vein categorizations are perfect. In order to assess the sensitivity of our simulated
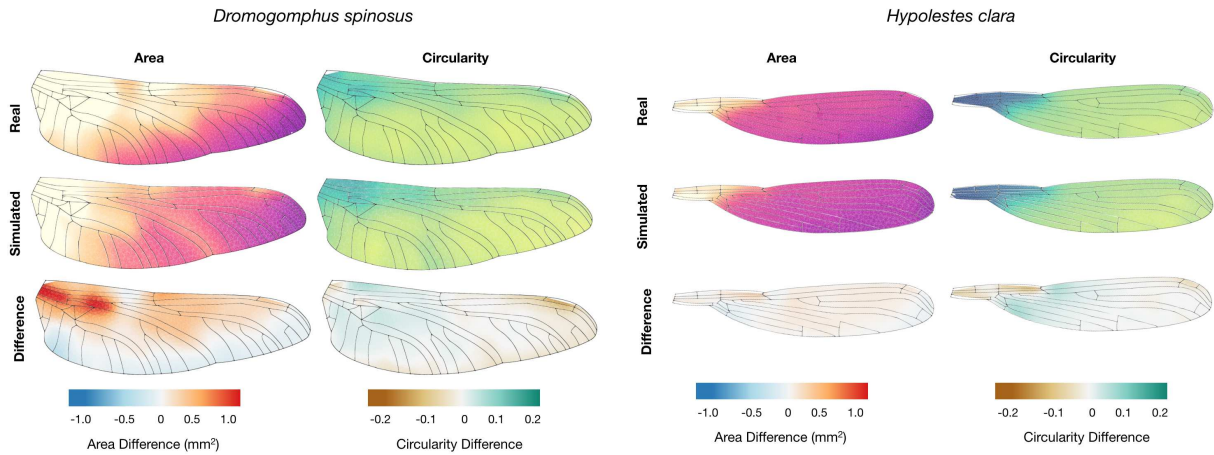
Figure S31: **Absolute error of the simulation.** Smoothed area and circularity maps for a real wing (top row) and model (middle row). The difference between these are shown in the bottom row.

results to our identification of primary veins, we take an example wing and simulated secondary veins under different sets of primary veins.

With each set of primary veins, we use them as region boundaries for our simulation approach as described in Section 3. Here, we assess several slightly different sets of primary vein identifications. In one case, we use just the primary veins named in [1] (Fig. S34, top row). The simulation captures most of wing effectively. In the middle part of the wing, however, simulated domains are slightly more circular than in the real wing.

In second case, we adapt the findings of Appel and Gorb (2014) [15]. Specifically, they show that in many species, long, straight veins also have microscopic cuticular structures that are shared in common with the conserved veins defined by Needham [1, 15]. Under the assumption that shared cuticular morphology indicates shared primary vein identity, we increase the set of primary veins using Appel and Gorb's findings as a guide. In doing so, we improve the performance of the vein simulation (Fig. S34, second row).

Lastly, we show that we can randomly perturb the identifications of primary veins without severely influencing the results of the model. As described above, our approach for simulating secondary veins involves equilibrating the positions of inhibitory seeds in closed regions. Thus, after identifying primary veins, we connect unconnected ends in order to close all regions. We do so by joining each unconnected end to the closest primary vein neighbor (Section 3.1.1). In the bottom third and fourth rows of Fig. S34, we remove some primary veins and alter how we connect unconnected vein ends. This shows that the specifics of these choices do not greatly influence our results.

5   Availability of data and code

Integer csv files of segmented images of all data along with code used in the manuscript are freely available. All code and data can be found at http://seas.harvard.edu/~chr/wing_data/.
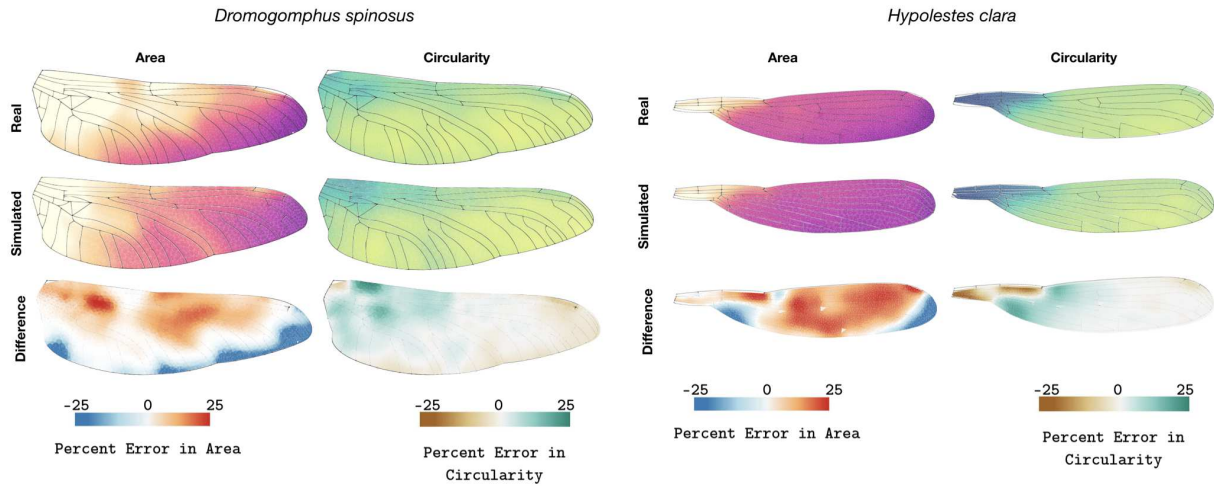
Figure S32: **Relative error of the simulation.** Smoothed area and circularity maps for a real wing (top row) and model (middle row). The difference between these are shown in the bottom row, where percent error is plotted.

5.1 Dragonfly wing data

In Fig. S35, we show segmented and polygonized plots of every dragonfly used in the manuscript colored by size and circularity.

A high quality version of this image is available at: http://seas.harvard.edu/~chr/wing_data/Dragonfly_Wing_Aug_14.png [157.8 MB]

5.2 Damselfly wing data

In Fig. S36, we show segmented and polygonized plots of every damselfly used in the manuscript colored by size and circularity.

A high quality version of this image is available at: http://seas.harvard.edu/~chr/wing_data/Damselfly_Wing_Aug_14.png [28.4 MB]

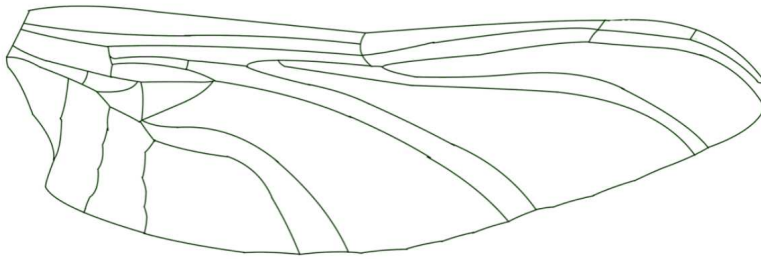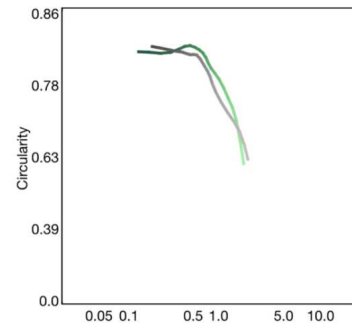## Area

Circularity

-50%   Percent Error   50%
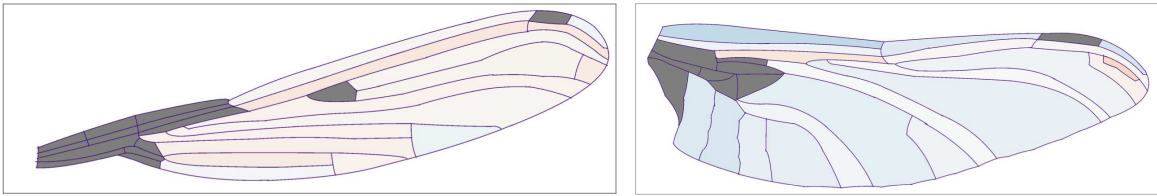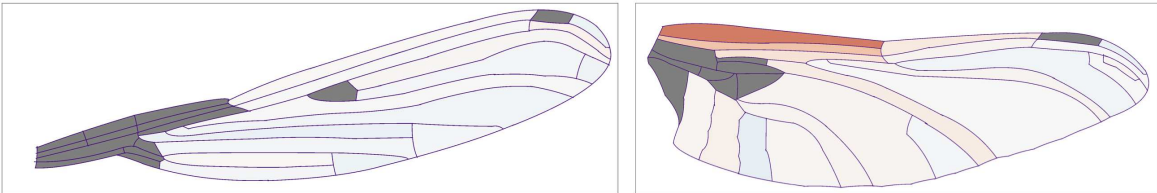
Figure S33: **Error of the model by region.** For each region bound by primary veins of a damselfly and dragonfly, we have plotted the relative error.
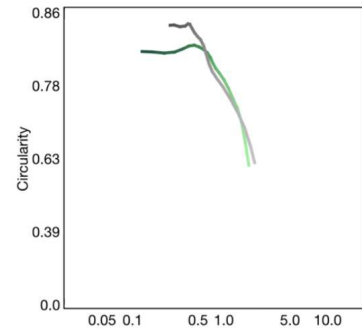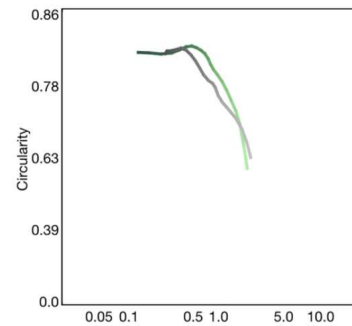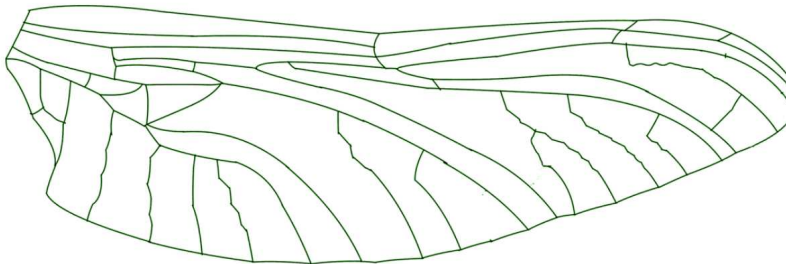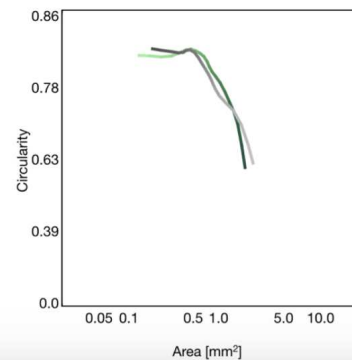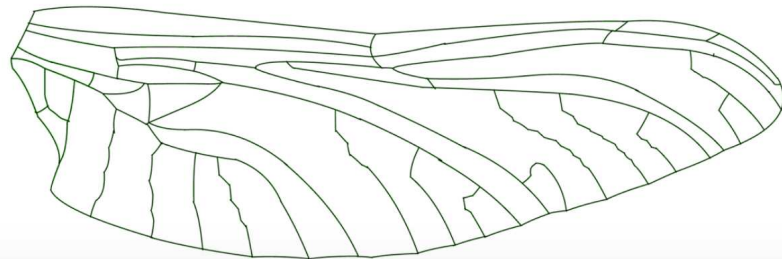
Figure S34: **Effect of region boundaries on trace.** Four different region boundaries and their corresponding P–D wing traces. The wing is an *Arigomphus villosipes*. The wing is 32.5 mm long. In the top row, we identify primary veins as those indicated as broadly conserved in Needham 2014 [1]. In the second row, we show veins adapted from Appel and Gorb 2014 [15] where they assessed veins for a variety of cuticular structures and found a subset of veins that have common features. In the bottom two rows, we begin with the set of primary veins shown in the second row, alter some primary veins, and then randomly alter the connections formed in linking the unconnected vein ends. The simulated P–D wing traces are shown in grey; real wing traces are shown in green.

Figure S35: All dragonflies used in the manuscript, colored by size and circularity.
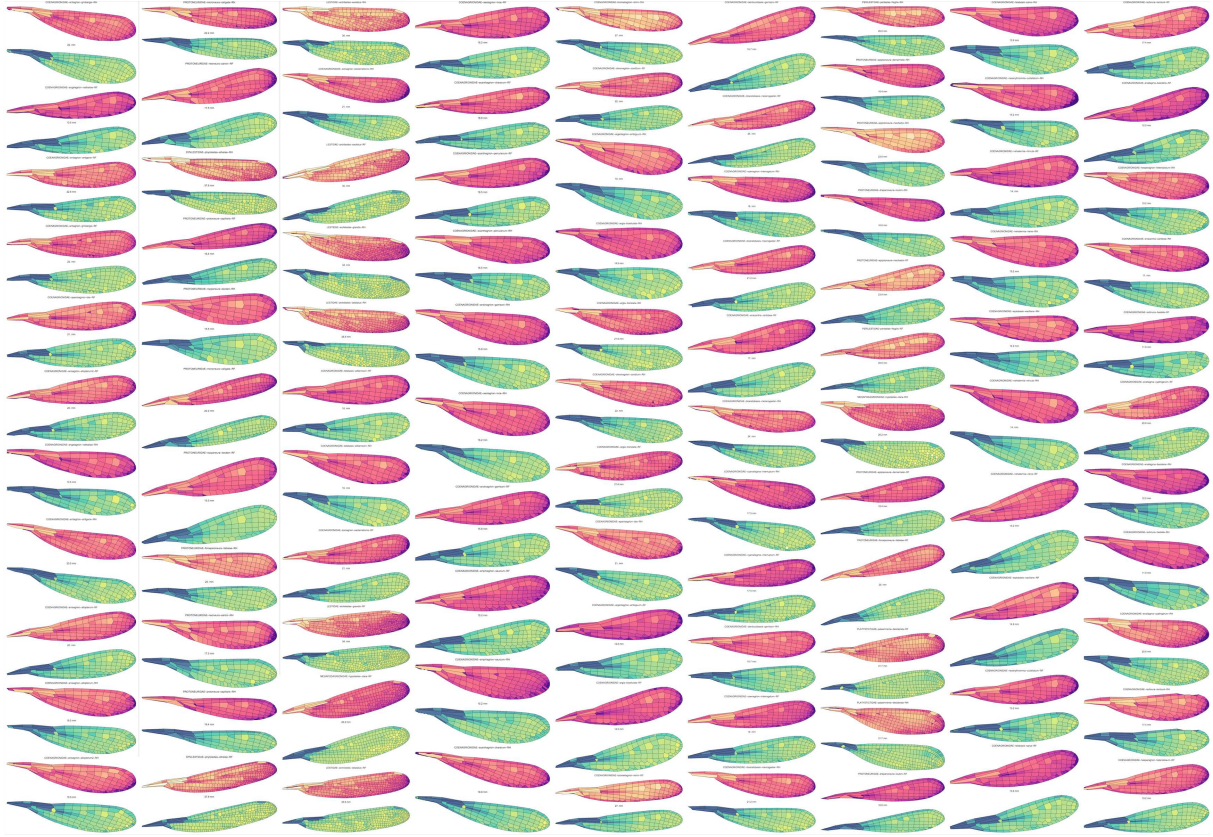
Figure S36: All damselflies used in the manuscript, colored by size and circularity.

References

[1] Needham, J. G., Westfall, M. J., and May, M. L. *Dragonflies of North America: the Odonata (Anisoptera) fauna of Canada, the continental United States, northern Mexico and the Greater Antilles.* Third edition, Gainesville, FL: Scientific Publishers. 2014.

[2] Garrison, R.W., von Ellenrieder, N., and Louton, J. A. *Dragonfly genera of the New World : an illustrated and annotated key to the Anisoptera.* Baltimore, MD: JHU Press. 2006.

[3] Kukalova-Peck, R. *Origin and Evolution of Insect Wings and Their Relation to Metamorphosis, as Documented by the Fossil Record.* J. Morph. 156, 53–126 (1978).

[4] Wootton, R. *Function, homology and terminology in insect wings.* Systematic Entomology 4, 81–93 (1979).

[5] Carpenter, F. M. *The Lower Permian insects of Kansas. Part 11.* Psyche, Cambridge, 73, 46–88 (1966).

[6] Béthoux, O. *Wing venation pattern of Plecoptera (Insecta: Neoptera).* Illiesia 1(9), 52–81 (2005).

[7] Westfall, M. J. , May, M. L *Damselflies of North America.* Third edition, Gainesville, FL: Scientific Publishers. 1996.

[8] Donoughe, S., Crall, J. D., Merz, R. A., and Combes, S. A. *Resilin in Dragonfly and Damselfly Wings and Its Implications for Wing Flexibility.* Journal of Morphology 272, 1409–1421 (2011).

[9] Garrison, R.W., von Ellenrieder, N., and Louton, J. A. *Damselfly genera of the New World : an illustrated and annotated key to the Zygoptera.* Baltimore, MD: JHU Press. 2010.

[10] Sommer, C., Strähle, C., Köthe, U., and Hamprecht, F. A. *ilastik: Interactive Learning and Segmentation Toolkit.* Eighth IEEE International Symposium on Biomedical Imaging (ISBI). Proceedings, 230–233 (2011).

[11] Cilla, R., Mechery, V., Hernandez de Madrid, B., Del Signore, S., Dotu, I., and Hatini, V. *Segmentation and Tracking of Adherens Junctions in 3D for the Analysis of Epithelial Tissue Morphogenesis.* PLoS Comput. Biol. 11(4), e1004124 (2015).

[12] Heller, D., Hoppe, A., Restrepo, S., Gatti, L., Tournier, A. L., Tapon, N., Basler, K., and Mao, Y. *EpiTools: An Open-Source Image Analysis Toolkit for Quantifying Epithelial Growth Dynamics.* Development Cell 36, 103–116 (2016).

[13] Etournay, R., Merkel, M., Popović, M., Brandl, H., Dye, N. A., Aigouy, B., Salbreux, G., Eaton, S., and Jülicher, F. *TissueMiner: A multiscale analysis toolkit to quantify how cellular processes create tissue dynamics.* eLife 5, e14334 (2016).

[14] Lamprecht, M. R., Sabatini, D. .M., Carpenter, A. E. *CellProfiler: free, versatile software for automated biological image analysis.* BioTechniques 42, 71–75 (2007).

[15] Appel, E. and Gorb, S. N. *Comparative functional morphology of vein joints in Odonata.* Zoologica. 159, (2014).

[16] Hamilton, K. G. Andrew *The Insect Wing, Part III. Venation of the Orders.* Kansas Entomological Society. Vol. 45 No. 2, (1972).

[17] Osher, S. and Sethian, J. A. *Fronts Propagating with Curvature Dependent Speed: algorithms Based on Hamilton–Jacobi Formulations.* J. Comput. Phys. 79, 12–49 (1988).

[18] Chopp, D. *Some Improvements of the Fast Marching Method.* SIAM J. Sci. Comput. 23(1), 230–244 (2006).

[19] https://github.com/scikit-fmm/scikit-fmm

[20] Encyclopedia of Life. Available from http://www.eol.org. Accessed August 2017.

[21] Kesel, A. B. *Aerodynamic Characteristics of Dragonfly Wing Sections Compared With Technical Aerofoils.* The Journal of Experimental Biology 203, 3125–3135 (2000).

[22] Jongerius, S. R., and Lentink, D. *Structural Analysis of a Dragonfly Wing.* Experimental Mechanics 50, 1323–1334 (2010).

[23] Wikimedia Commons, John Tann, CC BY 2.0 https://en.wikipedia.org/wiki/Petalura_gigantea#/media/File:Petalura_gigantea_female_wings_(34921024531).jpg Accessed Sept. 18, 2017.

[24] Wikimedia Commons, John Tann, CC BY 2.0 https://en.wikipedia.org/wiki/Petalura_ingentissima#/media/File:Petalura_ingentissima_female_wings_(34665011080).jpg Accessed Sept. 18, 2017.

[25] Wikimedia Commons, John Tann, CC BY 2.0 https://en.wikipedia.org/wiki/Ictinogomphus_dobsoni#/media/File:Ictinogomphus_dobsoni_male_wings_(34928349381).jpg Accessed Sept. 18, 2017.

[26] Wikimedia Commons, John Tann, CC BY 2.0 https://en.wikipedia.org/wiki/Blue-spotted_hawker#/media/File:Adversaeschna_brevistyla_female_wings_(34888576182).jpg Accessed Sept. 18, 2017.

[27] Wikimedia Commons, John Tann, CC BY 2.0 https://en.wikipedia.org/wiki/Gynacantha_dobsoni#/media/File:Gynacantha_dobsoni_male_wings_(35019600076).jpg Accessed Sept. 18, 2017.

[28] Wikimedia Commons, John Tann, CC BY 2.0 https://en.wikipedia.org/wiki/Cordulephya_montana#/media/File:Cordulephya_montana_female_wings_(34927994381).jpg   Accessed Sept. 18, 2017.

[29] William H. Press, Saul Teukolsky, William T. Vetterling, and Brian P. Flannery *Numerical Recipes: The Art of Scientific Computing* Third Edition (2007), 1256 pp. Cambridge University Press.

[30] Lloyd, S. P. *Least squares quantization in PCM.* IEEE Transactions on Information Theory 28(2), 129–137 (1982).

[31] Tillyard, R. J. *Fauna of British India. Odonata. Volume 2: On an Anisozygopterous Larva from the Himalayas (Order Odonata).* Records of the Indian, 93–107 (1921).

[32] http://matteich.photoshelter.com/image/I00004Z1IRt8Yx.Q

[33] Simone, R. P. and DiNardo, S. *Actomyosin contractility and Discs large contribute to junctional conversion in guiding cell alignment within the Drosophila embryonic epithelium.* Development, 1385–94 (2010).

[34] https://commons.wikimedia.org/wiki/File:Osborn_1912_trachodon_scale_pattern.png

[35] http://www.publicdomainpictures.net/pictures/130000/velka/giraffe-skin-pattern-14425724840w4.jpg

[36] http://4.bp.blogspot.com/_RqNCCCrU4dw/TK2LmG2wchI/AAAAAAAAAMY/px1VwYGsThU/s1600/uarnak.jpg

[37] De Celis, José F. and Diaz-Benjumea, Fernando J. *Developmental basis for vein pattern variations in insect wings* The International Journal of Developmental Biology, 653–664 (2003).

[38] Blair, Seth S. *Wing vein patterning in Drosophila and the analysis of intercellular signaling* Annual Review of Cell and Developmental Biology, 293–319 (2007).

[39] Combes, S A and Daniel, T. L. *Flexural stiffness in insect wings I. Scaling and the influence of wing venation* The Journal of experimental biology, vol 206. No 17. (2003).

[40] Combes, S. and Daniel, T. *Flexural stiffness in insect wings II. Spatial distribution and dynamic wing bending* The Journal of experimental biology, (2003).

[41] Stark, J. and Bonacum, J. and Remsen, J. and DeSalle, R. *The evolution and development of dipteran wing veins: a systematic approach* Annual review of Entomology, vol 44. (1999).

[42] Lehmann, Fritz-Olaf and Gorb, Stanislav and Nasir, Nazri and Schützner, Peter *Elastic deformation and energy loss of flapping fly wings* The Journal of experimental biology, vol 214. (2011).

[43] Mountcastle, Andrew M. and Combes, Stacey A. *Biomechanical strategies for mitigating collision damage in insect wings: structural design versus embedded elastic materials* The Journal of Experimental Biology, vol 217. (2014).

[44] Gorb, Stanislav N. *Serial elastic elements in the damselfly wing: mobile vein joints contain resilin* Naturwissenschaften, vol 86. (1999).

[45] Appel, Esther and Gorb, Stanislav N. *Resilin-bearing wing vein joints in the dragonfly Epiophlebia superstes* Bioinspiration & Biomimetics, vol 6. (2011).